COMPARISON OF RESULTS USING THE FINE RESOLUTION ENVIRONMENTAL HYDRODYNAMIC MODEL WITH LABORATORY PIV ANALYSIS OF VORTEX DYNAMICS FOR SHALLOW TIDAL INLETS

A Thesis

by

KATIE LYNN HUTSCHENREUTER

Submitted to the Office of Graduate and Professional Studies of
Texas A&M University
in partial fulfillment of the requirement for the degree of

MASTER OF SCIENCE

Chair of Committee,	Scott Socolofsky
Committee Members,	James Kaihatu
	Robert Hetland
Head of Department,	Robin Autenrieth

May 2017

Major Subject: Civil Engineering

ABSTRACT

Tidal flows through inlets with vortex formation have long been of great environmental importance. The transport mechanisms between the bay and the ocean must be well understood to correctly predict the transport of sediment, pollutants, or living organisms. The results from the 3D Fine Resolution Environmental Hydrodynamic (FREHD) model with a hydrostatic pressure assumption and a one equation turbulence model are compared with experimental measurements of surface velocities. The one equation turbulence model was proven to be essential to the model performance. A constant viscosity turbulence model gave poor results in comparison to the experimental data. The FREHD model is able to predict the characteristics of the primary starting-jet vortices with relative accuracy including the trajectory and size of the vortex. The model has limitations on grid resolution which does not allow the high swirl strength in the center of the vortex or any secondary vortices formed by boundary layer separation from the inlet boundary to be predicted by the model. In the experimental data, secondary vortices form and eventually contribute to the total circulation within the primary vortex. Vortices with low circulation also decay faster than observed. The model is able, however, to predict the total circulation well during parts of the tidal cycle when the experimental data does not show secondary vortex formation. A third order upwind advection scheme improved the results of the FREHD model and allowed for higher swirl strength values which increased the amount of total circulation within the primary vortices.

ACKNOWLEDGMENTS

The modeling portion of the research in this thesis was funded by the Texas General Land Office under a grant entitled ”Improving oil spill predictions near shore and across the bay/coastal interface”. The laboratory experiments used for model validation were funded by the International Research and Education in Engineering Program (IREE) under the National Science Foundation, project number CBET-0637034 and were conducted at the University of Karlsruhe, Germany.

I would like to thank my Advisor, Dr. Scott Socolofsky as well as the other two members of my thesis commitee, Dr. James Kaihatu and Dr. Robert Hetland for their input. Also, Dr. Ben Hodges from the University of Texas for developing the model used for this work as well as his guidance and input. Next, thanks to Duncan Bryant and Kerri Whilden for performing the laboratory experiments and the analysis of the laboratory data which was used for this thesis.

Finally, thanks to my family for their continuous love and support through my entire time at Texas A&M University.

CONTRIBUTORS AND FUNDING SOURCES

Contributors

This work was supported by a thesis committee consisting of Professor Scott Socolofsky and Professor James Kaihatu of the Department of Civil Engineering and Professor Robert Hetland of the Department of Oceanography.

The data analyzed for Chapter 5 was provided by Professor Scott Socolofsky. The analyses depicted in Chapter 5 were conducted in part by Kerri Whilden and Duncan Bryant and were published in 2012 in an article listed in Environmental Fluid Mechanics.

All other work conducted for the thesis was completed by the student independently.

Funding Sources

Graduate study was supported by a fellowship from Texas A&M University and a research fellowship from Texas General Land Office.

NOMENCLATURE

TAMU	Texas A&M University
ADCP	Acoustic Doppler Current Profiler
CTD	Conductivity, Temperature, Depth
PPM	Propeller Meter
ADV	Acoustic Doppler Velocimeter
PIV	Partical Image Velocimetry
FREHD	Fine Resolution Environmental HydroDynamic model

TABLE OF CONTENTS

LIST OF FIGURES

LIST OF TABLES

1 INTRODUCTION AND LITERATURE REVIEW

Tidal flow between an estuary and the open ocean leads to the formation of large-scale two-dimensional eddies, which enhance or diminish tidal flushing and mixing. These eddies, also known as starting-jet vortices, have been studied extensively through field [23, 18, 8, 20] and laboratory experiments [11, 12, 21, 14, 5]. Substantial work has been done to understand the formation and propagation of these vortices through highly idealized inlets [14] as well as vortices affected by growing channel lengths [5]. Numerical modeling has been used to try to capture starting-jet vortex formation in the field [4, 17] but the amount of available data is the limiting factor for validation. For field scale models, it is unlikely that there exists validation data beyond a few points in the domain. Although numerical modeling of laboratory experiments has been done to study the flow around a headland [19, 7], this paper aims to run a numerical model that mirrors laboratory experiments that studied flow through an inlet to gain knowledge about the model components necessary to capture starting-jet vortex behavior within a numerical model.

Laboratory experiments have been widely used to study the formation of starting-jet vortices. Visualization tools such as dye and passive tracers are used in order to identify and analyze vortex properties. Kawashi et. al. was the first to visualize vortex formation through an inlet. He determined that the vortex behavior depends on the Strouhal number and then separated the vortex behavior into three distinct groups based on the movement

of the vortex throughout a tidal period. Type I vortices remained stationary at the mouth of the inlet through the entire tidal period. Type II vortices however, become entrapped in the inlet on reverse tide, while type III vortices were able to escape the inlet mouth before the start of reverse tide [11, 12]. Wells and Van Heijst expanded on the understanding of vortex formation by quantifying a critical value of the Strouhal number defined by

$$K_w = \frac{W}{U_{max}T} \tag{1.1}$$

where W is the width of the channel, U_{max} is the maximum channel velocity and T is the tidal period. The vortices were shown to propagate away from the inlet if this value was less than 0.13. If the value was equal to the critical value, the vortices remained stationary, and if the value exceeded it, the vortices became entrapped during the reverse tide. This experiment did not include three-dimensional or bottom friction effects since stratification was used in the laboratory experiment in order to make the flow quasi two-dimensional [21].

Unlike Wells and Van Heijst, the experiment by Nicolau del Roure et al. at the University of Karlsruhe, Germany did not attempt to limit three-dimensional effects. They used dye to visualize the three types of vortices as well as Particle Image Velocimetry (PIV) to analyze the vortex kinematic characteristics. Vortices were identified in the PIV analysis and the position, equivalent circular diameter, maximum vorticity, and circulation of each vortex were determined. Since the three-dimensional effects were not constrained, the vorticity and circulation decreased gradually as the vortex propagated away from the

inlet due to bottom friction, but the size was relatively unaffected. The resulting K_w for a stationary vortex was 0.11 which aligned well with the accepted critical value of 0.13 [14].

Whilden et al. [22] analyzed the characteristics of starting-jet vortex formation through an idealized inlet with varying water depth. Three, five, and nine centimeter water depths were used during the experiments. The non-dimensional behavior, such as position and size, of the vortices were similar for the five and nine centimeter cases. The three centimeter case behaved differently, likely due to increased bottom friction effects.

Bryant el al. [5] conducted a similar experiment to Nicolau del Roure et al. but focused on Type III vortex behavior. The experiments investigate the effect of channel length on vortex formation. When the channel length becomes on the order of or larger than the channel width, an understanding of the lateral boundary layer becomes important in studying the vortex behavior. There is an additional vortex that forms aside from the starting-jet vortex during the reverse tide called the expelled boundary layer vortex. Bryant et al. was able to analyze the starting-jet vortex behavior with the presence of an expelled lateral boundary layer. He was also able to track both the starting-jet vortex and the expelled boundary layer vortex using dye visualization and Particle Image Velocimetry.

Bryant et al. [5] determined that an expelled boundary layer vortex is not present during every tidal cycle. The presence of an expelled boundary layer vortex can affect the behavior of the starting-jet vortex in two distinct ways. Mode 1 occurs when the expelled boundary layer vortex is small in comparison to the starting jet vortex. In this case, the presence of the expelled boundary layer vortex causes the starting jet vortex to propagate

away from the inlet at a 35 degree angle, but the expelled boundary layer vortex quickly dissipates. Mode 2 occurs when the expelled boundary layer vortex and starting-jet vortex have similar sizes. This causes both vortices to form a dipole and propagate quickly away from the inlet at a 20 degree angle [5]. The PIV laboratory results from Case B and F of this study are part of the data set used for comparison to the model results in this thesis.

Numerical modeling is also a powerful tool in studying starting-jet vortex formation. Lopez-Sanchez et al. [13] studied vortex formation through field scale inlets by solving the equations of motion using a pseudo spectral code based on Chebyshev polynomial for spatial coordinates and a second-order finite difference method for time. He then analyzed vortex characteristics such as speed, intensity, and stability. He tested the dependence of the Strouhal number and the Reynolds number as well as interaction between the vortices. Bellafiore and Umgiesser also studied the small scale processes occurring near inlets in the Venice Lagoon using a 3D shallow water hydrodynamic finite-element model and compared the results to an hourly HF radar dataset of surface currents over a 13-month period. The dataset is the result of three antennas, two located on the coast and one located 15 km offshore. The model was used to investigate the influence of different forcing including tides, freshwater inflow, and winds independently. They modeled the conditions during each month HF radar data was available and studied the conditions necessary for vortex formation. Once the HF radar data was processed it was interpolated onto a regular grid of size 750 m. Because of the low spatial resolution of the HF radar data, the vortices produced from the model could not be verified by the field data [4].

Numerical modeling has also been used to study the flow around a headland which produces similar vortex formation during tides as flow through an inlet. Signell and Geyer studied the flow around a headland using analytical and numerical models [17]. They identified three parameters that affected the occurrence of vortices. The parameters included the geometry of the headland, far-field magnitude and frequency of the tidal flow, and the depth averaged drag coefficient. Two-dimensional, depth-averaged simulations were run to test the sensitivity to these three parameters. As bottom friction decreased, there was either no separation at the headland, only one eddy existed at a time, or the eddies interacted with each other if bottom friction was weak enough. More recently, other models have been run to study the flow around headlands. Two-dimensional depth averaged models have been used [16, 3] as well as 3-dimensional modeling [2]. These models solve the same equations using different numerical schemes. They show qualitative comparisons to data but until recently there were no quantitative comparisons.

In 2013, Draper et al. compared results of a depth-averaged numerical model to experimental data in order to study the energy extraction of a turbine placed near the tip of a headland [7]. The laboratory experiments measured water surface elevation, water velocity using Propeller Meters (PPMs) and Acoustic Doppler Velocimeters (ADVs), and drag force on the tidal device emulators. The numerical model was depth-averaged and ignored any viscous effects. When comparing the experimental results and the numerical model, the results showed that the numerical model could provide reasonable predictions of force on the turbines as long as the turbine is not in the wake of another coastal structure. Al-

though the model performed well, it tended to underestimate the velocity deficit behind the turbine. They also tested the sensitivity to the drag coefficient, inlet velocity at mid-depth, and the water depth within the numerical model. They determined that bed friction was most likely to be the most uncertain input but that the model was the most sensitive to the inlet velocity input.

Stansby et al. also compared numerical model results to experimental data [19]. They used a 3D, hydrostatic numerical model with $k-\varepsilon$ turbulence modeling. The model used was TELEMAC-3D. All models to this point define bed shear with a constant drag or shear coefficient. This model differs because the bed shear stress is implicit and is part of the boundary layer computation. The experimental data included surface velocities for the flow around a headland in a laboratory tank with an exaggerated vertical scale and a water depth of 0.48m. The velocities were compared at various points around the headland for different Kuelegan-Carpenter (KC) and Reynolds numbers. The velocities near the headland were the focus of this study because of possible tidal stream turbine deployment. The expected vortices near the headland formed in both the model and the experimental data but were not analyzed any further. The velocities predicted by the model were better near the headland than within the recirculation zones or vortices.

Comparison of numerical models to experimental data allows for a comparison to data with controlled conditions and extremely high resolution compared to field data. This thesis aims to compare the results of the Fine Resolution Environmental Hydrodynamic (FREHD) model to laboratory experiments from Bryant et al. [5] and Whilden et al. [22]

to understand the necessary model components needed to capture the vortex formation through an inlet. Although numerical models of flow around a headland have been compared to experimental data, only velocity comparisons were made. Comparisons of velocities is important in assessing the accuracy of a model, but there are other characteristics of the flow that can help analyze the model's ability to resolve the formation of starting jet vortices, including vortex properties such as size, position, and circulation.

The remainder of this thesis is structured as follows. First the laboratory setup is presented, followed by an introduction to the FREHD model. Then, the model is calibrated to best represent the laboratory setup, and a sensitivity study to various model parameters is presented. Next, the experimental results are compared to the results of the FREHD model, and finally a summary and conclusion is provided.

2 EXPERIMENTAL METHODS

Both laboratory experiments and a numerical model were used in order to capture vortex formation and propagation at the mouth of shallow tidal inlets. The laboratory experiments were setup based on three criteria: the Froude Number scaling, the shallow water assumption, and the inlet Strouhal number. Cameras and semi-buoyant tracers were used to capture and analyze the flow over multiple tidal periods. The numerical model was then designed to replicate the laboratory experiments as closely as possible. The following sections will outline the setup of both the laboratory experiments and the numerical model.

2.1 Laboratory Experiments

All laboratory experiments were conducted in the shallow water basin at the Institute of Hydromechanics at the University of Karlsruhe in Karlsruhe, Germany. The basin is 15 meters long and 5.5 meters wide and can generate flow in either direction along the long axis of the basin using a variable-speed pump. The pump provides the flow into the basin through a diffuser system. The diffuser system includes flow straighteners and surface wave dampers resulting in a uniform flow across the width of the basin. The bottom of the basin is smooth to +/- .7 mm with a sand roughness (k_s) of 0.1 millimeters.

A total of six inlet configurations were run in the tank described above. The three configurations which this thesis will focus on are an idealized inlet, a large barrier island, and a long jetty. The first and simplest configuration is an idealized inlet [Figure 2.1]. The

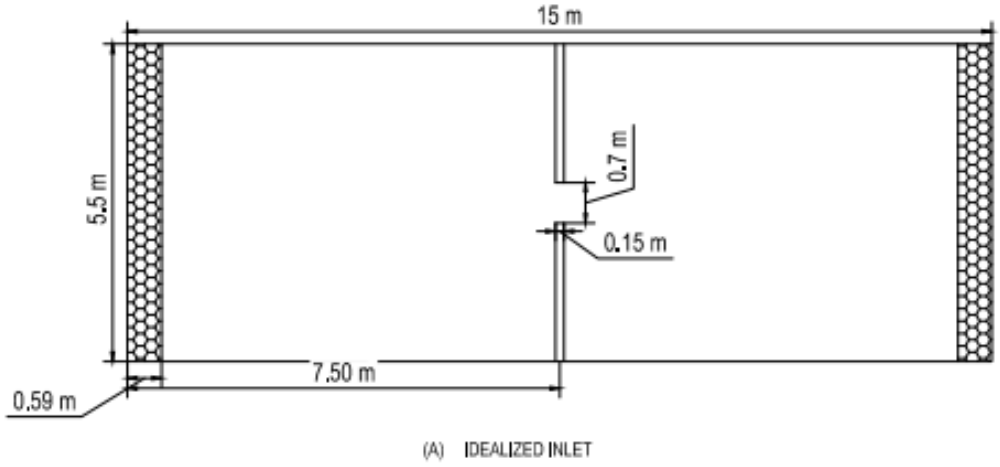

Figure 2.1: Schematic of Shallow Water Wave Basin at University of Karlsruhe with idealized inlet configuration

inlet was constructed with an inlet width, W, of 0.79 m. The inlet channel length is 0.15 m to minimize the boundary layer. This experiment was performed for 3, 5, and 9 centimeter water depths. The 5 and 9 centimeter cases operated the pump at 10% of its maximum speed and the pump was decreased to 7% of its maximum speed for the 3 cm cases.

When the configuration is changed to a large barrier island or long jetty, a boundary layer along the channel plays an increasing role on the vortex formation [Figure 2.2 (B);(C)]. Both the large barrier island and long jetty cases were constructed with an inlet width, W, of 0.94 m. The inlet channel length was increased to 1.35 m for the large barrier island case and to 1.11 m for the long jetty case. These cases no longer attempt to minimize the boundary layer like the idealized inlet case. Instead, these cases allow for the analysis of vortex formation with the introduction of a relatively large boundary layer in the channel. Both the large barrier island and long jetty cases were conducted with a 5 centimeter water depth. For all configurations, tidal forcing was replicated in the experiment by sinu-

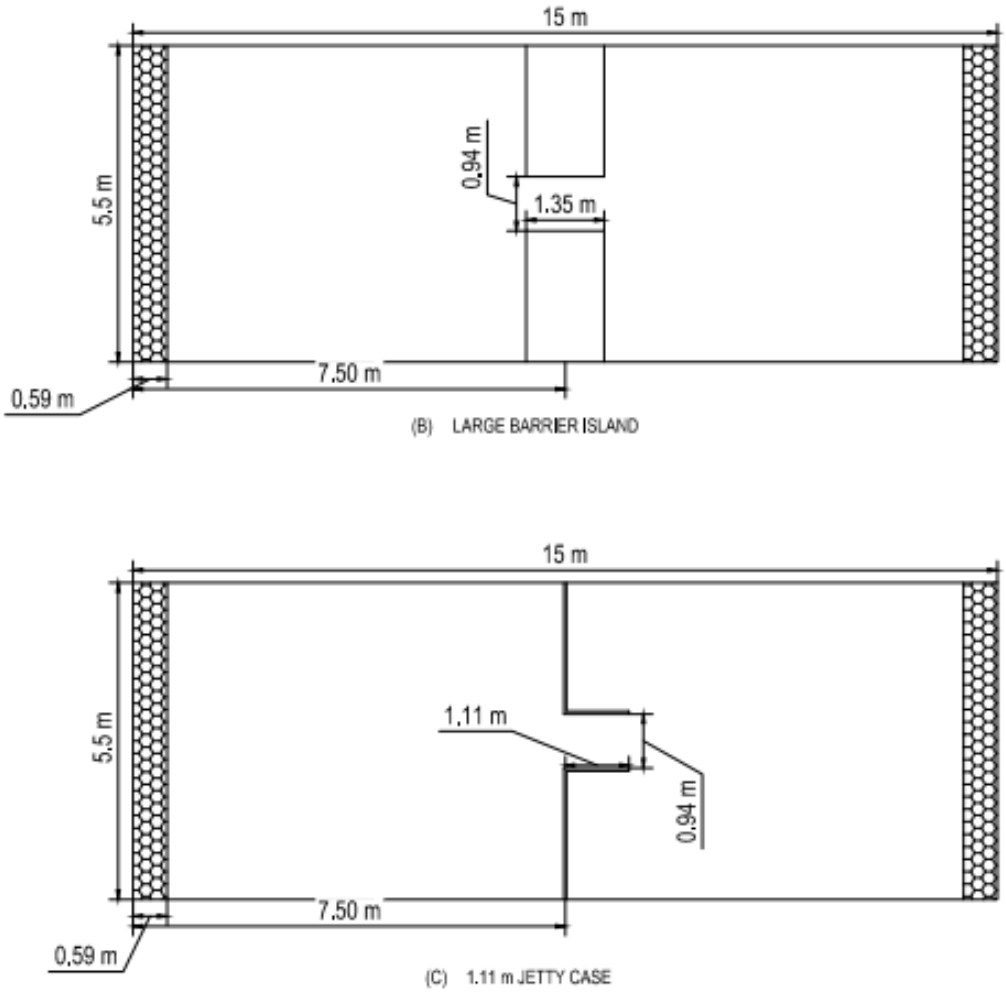

Figure 2.2: Schematic of Shallow Water Wave Basin at University of Karlsruhe with (B) long barrier island and (C) long jetty configurations

soidally varying the pump flow. All experiments were conducted using a 50 second tidal period; after 25 seconds the flow was reversed using a system of valves. The experiments were run for at least 4 tidal periods resulting in a total time of approximately 200 seconds for each experiment.

Two cameras were mounted above the basin and captured the flow on one side of the inlet with a 10% overlap. Semi-buoyant tracers were used to visualize the flow, and the

particle motion was then analyzed using Particle Image Velocimetry (PIV). PIV uses the locations of the particles in consecutive frames and the frame rate to calculate a velocity field for the data. The velocity fields were extracted from the PIV data and then used to analyze the starting-jet dipoles that formed at the mouth of the inlet. The grid size of the velocity fields is determined from the window size chosen for the PIV analysis. In order to use PIV analysis, the program must search the image within two consecutive frames, the window size specifies the size of the search window and then calculations can be made based on the experimental setup to determine the number of pixels per centimeter. A 32x32 pixel window size was used with a 50% overlap for the PIV analysis. This resulted in a grid size of approximately 2.36x2.36 cm for the final velocity fields. Characteristics of the vortices such as swirl strength, vorticity, spin-up time, and vortex diameter were calculated from the velocity fields. Key features from the velocity fields were also exported from the PIV data in order to gain adequate information to set up the numerical model. This included the average velocity through the inlet, which was not measured during the laboratory experiments but was calculated from the PIV analysis.

2.2 Numerical Model

The numerical model chosen for the analysis of these laboratory experiments is the Fine Resolution Environmental HydroDynamic or FREHD model. Here, the main characteristics of the model are presented along with the model setup for this work. Further information on the FREHD model can be found on Ben Hodges page of the University of

Texas at Austin Center for Research in Water Resources website.

2.2.1 Model Description

FREHD is a Matlab-based hydrodynamics model developed by Prof. Ben Hodges at the University of Texas at Austin. FREHD uses a hybrid finite-difference/finite volume formulation in a semi-implicit predictor/corrector scheme. The Tidal Residual Intertidal Mudflat (TRIM) model by Casulli and the Estuary and Lake Computer Model (ELCOM) by Hodges were the contributing models to developing FREHD. The approach follows Casulli and Zanolli. The model has the ability to run with three different advective schemes. The first is a first order upwind scheme which is used for the majority of the model runs. A discussion of the other two possible advection schemes are described in Section 5.3. They include a third order upwind scheme and a second order centered scheme.

2.2.2 Model Setup

When using FREHD, the user can provide a variety of input files in order to define the parameters of the model run. The inputs considered when modeling this experiment were bathymetry, free surface elevation, number of vertical layers, and inflow boundary conditions. There are many other options for inputs to the FREHD model but they were not relevant to this experiment. Other possible inputs include wind, salinity, and tides, which may be useful when attempting to model field conditions, but for a laboratory setting, they were not necessary to include. FREHD also relies on configuration files to specify the control variables for the model run. The Default user settings file is read first by the code, that sets the settings for a particular system, that are rarely changed from run to run. The

user makes changes between different model runs in the User settings file.

Geometry

The computational domain is a standard, Cartesian, rectangular grid with uniform horizontal grid spacing throughout. The origin for the FREHD model is the upper left hand corner with x oriented positive downward and y oriented positive to the right. For the majority of the model runs, a relatively coarse grid was sufficient to resolve the features of interest. This model setup included 85 grid cells in the x-direction and 232 grid cells in the y-direction. When the grid is applied to the 5.5 by 15 m basin, the resulting grid size is 6.5 x 6.5 cm [Figure 2.3 (A)]. A fine grid was also used to test the effect of grid resolution on the model results. This model grid had 275 grid cells in the x-direction and 750 grid cells in the y-direction resulting in a 2 x 2 cm grid size [Figure 2.3 (B)]. When the grid was applied to the laboratory geometry, the origin was adjusted to match the origin used during the PIV analysis located at the inlet mouth. The coarse grid size in the x and y directions were chosen to give the best resolution with a reasonable computational time. A comparison of the model results from the coarse and fine grid cases are shown in Chapter 3.

In the vertical direction, the water column is divided into layers, each with a 5 mm thickness. The number of layers varies between 6 and 18, depending on the water depth. These conditions are represented by the bathymetry and vertical layer input files to the model. The location of the inlet is defined by setting the grid cells, at that location, to NaNs within the bathymetry file. The model also requires a layer of NaNs along the outer

edge of the grid. The model sensitivity to the number of vertical layers is shown in Chapter 3.

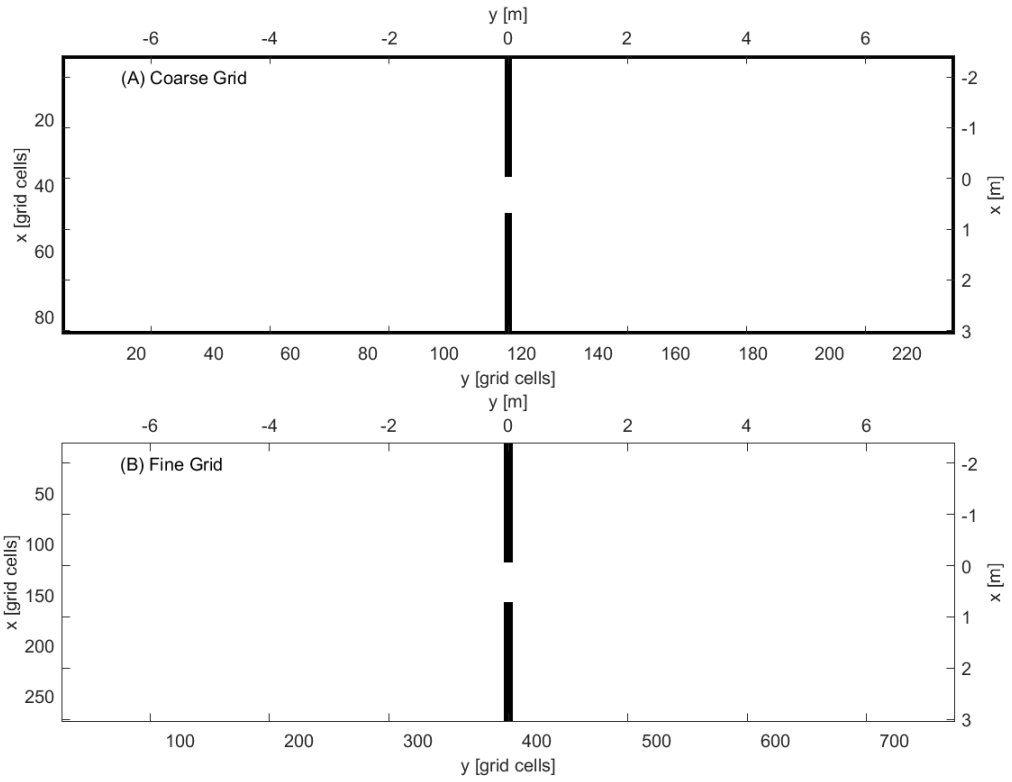

Figure 2.3: Model Grid Setup; (A) Coarse Grid Setup; (B) Fine Grid Setup

The elevation of the free surface is specified in another input file to the model. It is important to note that the elevation of the free surface is relative to the elevation of the bathymetry file not simply the depth at each grid cell location. For this experiment the free surface starts at a constant level equal to the water depth.

Inflow Conditions

The inflow is defined with an input file to the model that specifies the inflow locations and flow rate. The grid cell locations of the inflow for this experiment include all grid cells

on the far left and far right of the basin. The flow rate is specified using a matrix where the first column is time in seconds and the second column is flow rate in $\frac{m^3}{s}$. The flow rate is positive for inflow and negative for outflow. Since the pump varied sinosoidally for this experiment, the inflow in the minus y and plus y directions must reflect this pattern. The frequency (ω) of the sin wave is $\frac{2\pi}{T}$ where T is the tidal period. The frequency remained constant for all model runs. The amplitude (A) of the sine wave varied depending on the water depth and was adjusted until agreement with the average velocity through the inlet for the PIV data was reached. More details on this process can be found in Chapter 4. The inflow (Q_{in}) from the minus *y* side is given by

$$Q_{in} = A\sin(\omega t) \tag{2.1}$$

The inflow from the plus y side (Q_{out}) is the negative of Equ. 2.1 so that when there is inflow on the minus y side, there is outflow on the plus y side and vice versa. The inflow which showed the best agreement with the PIV data for each water depth is shown in Table2.1.

Table 2.1: Inflow Inputs to FREHD

Inlet Configuration	Water Depth [m]	Q_{in} $\frac{m^3}{s}$
Idealized	0.03	0.004
Idealized	0.05	0.007
Idealized	0.09	0.007
Large Barrier Island	0.05	0.012
Long Jetty	0.05	0.012

Time, *t*, in Equ. 2.1 is a vector of Matlab datenum values for each time step through-

out the model run. The time step chosen for the coarse grid model runs was 0.01 seconds in order to satisfy stability requirements imposed by the relationship between the grid size, the time step, and the maximum resulting velocity throughout a model run. The time step was decreased to 0.005 seconds for the fine grid case in order to maintain stability.

Friction

The two friction coefficients that must be specified within the FREHD model are the bottom friction coefficient and the sidewall friction coefficient. The bottom friction within the FREHD model is determined by a single coefficient of drag, C_D.This value was determined separately for each water depth following the approach of Chen and Jirka (1995). We start with the Swamee-Jain equation for friction factor, f, given by

$$f = 0.25[\log_{10}(\frac{k_s}{3.71h} + \frac{5.74}{Re^{0.9}})]^{-2} \tag{2.2}$$

where h is the water depth and k_s is the sand roughness. Re is the Reynolds number when the average velocity through the inlet is at a maximum and is given by

$$Re = \frac{U_{max}h}{\nu} \tag{2.3}$$

U_{max} is the maximum average velocity through the inlet from the PIV analysis of the laboratory data and ν is the kinematic viscosity. Then the coefficient of friction (C_f) was calculated using the relationship, $C_f = \frac{f}{4}$. C_D is then related to C_f by $C_D = \frac{1}{2}c_f$. The corresponding C_D values for each water depth are shown in Table 2.2.

Table 2.2: Friction Calculations for Model Setup

Water Depth [m]	U_{max} [m/s]	c_D
0.03	0.185	0.0051
0.05	0.269	0.004
0.09	0.211	0.0036

The sidewall friction coefficient was determined in a different manner. There is no known way to calculate the sidewall friction coefficient analytically so it was applied as a calibration parameter to the FREHD model. The model was run with identical input parameters but with three different values of the sidewall friction coefficient. The three values chosen were 0, 0.005, and 0.5. Both the model results and the physical knowledge of the laboratory setup were used to make an assessment of the best sidewall friction coefficient value to use. The model sensitivity to the sidewall friction coefficient is presented in Chapter 4.

Turbulence

Turbulence has been and still is a fundamental problem within computational fluid dynamics. The random nature of turbulence presents many problems when attempting to model the phenomenon. There are multiple ways to deal with the turbulence closure problem within the FREHD model. The first and simplest way is to specify a constant eddy viscosity for every point on the model grid. Although this method allows for the formation of tidal vortices, it is not a good representation of the flow in the laboratory. The model results using the constant viscosity turbulence model are presented in Chapter 4. In order to improve upon this, a more advanced turbulence model was chosen. The turbulence

model chosen solves one additional transport equation for the turbulent kinetic energy, k, given by

$$\frac{\partial k}{\partial t} + \frac{\partial}{\partial x_j}(U_j k) = R_{ij}\frac{\partial U_i}{\partial x_j} - \varepsilon + \frac{\partial}{\partial x_j}(\nu + \frac{\nu_t}{\sigma_k}\frac{\partial k}{\partial x_j}) \tag{2.4}$$

where σ_k is the closure coefficient known as the Prandtl-Schmidt number for k and R_{ij} is the Reynolds stress. The eddy viscosity (ν_t) and dissipation (ε) are given by

$$\nu_t = C_\mu \sqrt{k} l \tag{2.5}$$

$$\varepsilon = C_{me}\frac{\sqrt[3]{k}}{l} \tag{2.6}$$

The characteristic velocity scale is proportional to the square root of the turbulent kinetic energy which is denoted by k. C_μ and C_{me} are constants equal to 0.09 and 0.08 [10] respectively and l is the characteristic length scale. In this case, the length scale used within the model is the vertical layer thickness. For the dissipation calculation, l is equal to the vertical layer thickness for all grid cells. The eddy viscosity is calculated for both horizontal directions, x and y, as well as the vertical direction. For the horizontal eddy viscosity, l is also equal to the vertical layer thickness for all grid cells. For the calculation of the vertical eddy viscosity, l is equal to the vertical layer thickness for all grid cells except for the bottom layer. l for all grid cells in the bottom layer are equal to $\frac{1}{2}$ of the vertical layer thickness.

The two terms on the left hand side of Equ. 2.4 represent the rate of change of the turbulent kinetic energy. The first term on the right hand side is known as the production term. This term represents the specific kinetic energy per unit volume that an eddy will gain per unit time due to the mean strain rate. When modeling the k equation, the assumption is made that the Boussinesq eddy viscosity approximation is valid so the Reynolds stresses, R_{ij}, can be modeled by

$$R_{ij} = \nu_t(\frac{\partial U_i}{\partial x_j} + \frac{\partial U_j}{\partial x_i}) - \frac{2}{3}k\delta_{ij} \tag{2.7}$$

The second term on the right hand side is the dissipation given by Equ. 2.6. The final term combines the diffusion of turbulent energy by molecular motion, the turbulent transport of k, and the pressure fluctuation term.

When using the FREHD model, the three constants, C_μ, C_{me}, and l must be defined along with minimum values for the eddy viscosity, dissipation, and kinetic energy. The assumption was made that the eddy viscosity should not be less than the molecular viscosity, so the minimum values were set to $1 \times 10^{-6}\ \frac{m^2}{s}$.

3 THEORY

The PIV data and FREHD model output require post-processing in order to understand and compare the vortex properties. The following sections will outline the key parameters used to identify and compare the results.

3.1 Comparison of Model and Laboratory Data

The outputs from the FREHD model include velocities, turbulence variables, and depth. The velocities include the *x*, *y*, and *z* directed velocities at the faces for every grid cell as well as the *z* velocity at the surface. The turbulence variables include the *x*, *y*, and *z* viscosities as well as the production rate, dissipation rate, and kinetic energy used to solve the transport equation for the turbulent kinetic energy. The raw model output consists of 1 dimensional vectors for each variable which can then be manipulated to represent the 3 dimensional grid.

The first step in comparing the model and laboratory data is to interpolate to identical grids. The grid size for the PIV laboratory data is finer than the model output so the PIV laboratory data was interpolated to the model grid size. This allowed the laboratory and model data to be successfully compared. All further calculations were done using the velocity fields so the *x* and *y* velocities from the PIV laboratory data were interpolated to the model grid before any additional calculations were done. A standard two-dimensional linear interpolation was used for all PIV laboratory data. The PIV data was only inter-

polated within the PIV field of view and NaNs were used in Matlab to specify where no laboratory data is available. For the remainder of this thesis, all figures which show spatial representations of the data include the location of the end of the PIV field of view for reference.

3.2 Vortex Identification

Additional quantities were calculated in order to gain more information on vortex formation within a model run. The following section will explain the process used in order to calculate the vorticity, circulation, and swirl strength from the velocity outputs of the FREHD model.

3.2.1 Vorticity and Circulation

The circulation at a point (i, j) is determined by choosing a small rectangular contour around the point and using a standard integration scheme to calculate the local circulation. The circulation is then divided by the area of the region to arrive at an average vorticity in the area. The rectangular contour chosen uses the eight grid cells surrounding the grid cell at location (i, j). The average vorticity is defined by

$$(\bar{\omega}_z)_{i,j} = \frac{\Gamma_{i,j}}{4\Delta x \Delta y} \tag{3.1}$$

where Δx and Δy are the grid spacing in the x and y directions and $\Gamma_{i,j}$ is the circulation in the region given as

$$\begin{aligned}\Gamma_{i,j} = &\frac{1}{2}\Delta x(U_{i-1,j-1} + 2U_{i,j-1} + U_{i+1,j-1}) \\ &+\frac{1}{2}\Delta y(V_{i+1,j-1} + 2V_{i+1,j} + V_{i+1,j+1}) \\ &-\frac{1}{2}\Delta x(U_{i+1,j+1} + 2U_{i,j+1} + U_{i-1,j+1}) \\ &-\frac{1}{2}\Delta y(V_{i-1,j+1} + 2V_{i-1,j} + U_{i-1,j-1}).\end{aligned} \tag{3.2}$$

The vorticity and circulation were calculated for each grid cell and represent the local rotation of the fluid. These calculations follow the approach presented in "A Practical Guide to PIV Analysis". The total circulation within a given vortex was also calculated by taking a line integral over the contour which encloses the vortex

$$\Gamma_A = \oint_A (\bar{\omega}_z)_{i,j} dA \tag{3.3}$$

where Γ_A is the total circulation within the contour, $(\bar{\omega}_z)_{i,j}$ is the average vorticity for a given grid cell, and dA if the differential area or the grid size, given by dA= Δx Δy.

The vorticity was used to compare the laboratory and model results but was not used to identify the vortex location and size.

3.2.2 Swirl Strength

The local swirl strength criteria as defined by Adrian et al. [1] was used to identify vortices within a model or laboratory run. The calculation of the swirl strength requires the calculation of the spatial derivatives of the x-directed velocity, u, and the y-directed velocity, v. The spatial derivatives were calculated using a central difference approach

$$(\frac{df}{dx})_i = \frac{f_{i+1} - f_{i-1}}{2\Delta x}. \tag{3.4}$$

The central difference approach uses the point in front of and behind the point of interest to compute the derivatives yielding a second order accurate solution. The spatial derivatives were then combined to form the two-dimensional deformation tensor, D,

$$D^{2D} = \begin{bmatrix} \frac{du}{dx} & \frac{du}{dy} \\ \\ \frac{dv}{dx} & \frac{dv}{dy} \end{bmatrix} \tag{3.5}$$

and the swirl strength is calculated by finding the positive imaginary eigenvalues of the matrix in Equation 3.5.The swirl strength calculation isolates areas of local rotation without including the effects of local strain, unlike vorticity. The swirl strength is also independent of local rotation direction, so the swirl strength is at a maximum at the center of a vortex and decreases with distance.

3.3 Vortex Size and Location

The vortices were identified using the swirl strength criteria. A threshold swirl strength value of 0.2 $\frac{1}{s}$ was chosen for the PIV laboratory data in order to account for possible noise in the experiments. A contour for swirl strength equal to 0.2 $\frac{1}{s}$ was then identified as the boundary of the vortex. The vortex was assumed to be circular from inspection of the data so the area contained within the contour was calculated and then the diameter was determined from $A = \frac{\pi D^2}{4}$. The same approach was followed for the model results but the contour threshold chosen varied depending on the ratio of maximum swirl

strength in the PIV laboratory data versus the FREHD output.

$$Model_{thresh} = \frac{Lab_{thesh}}{Lab_{max}} Model_{max} \tag{3.6}$$

The Lab_{max} and $Model_{max}$ are the maximum swirl strength values over the length of the run for the PIV laboratory data and the FREHD model, respectively. They are known from the data. The Lab_{thresh} is the threshold of swirl strength which defines the boundary of the vortex and is chosen as $0.2\ \frac{1}{s}$. From these three variables the $Model_{thresh}$ was determined and used to define the edge of the vortex for the model output. The determined threshold from the model was used in the same manner as for the PIV laboratory data.

The location of the vortex was tracked by calculating the centroid of the contour described above. The spatial variability of the vortex was also compared using the location of maximum swirl strength within the vortex. These two locations are often different and give different insight into the vortex behavior.

3.4 Error

Root-mean-square (rms) error was the primary method of determining the amount of error between the model and laboratory results for time varying data. The rms error was calculated as

$$RMSE = \sqrt{\frac{\sum_{i=1}^{N} (\chi_{model} - \chi_{lab})^2}{N}} \tag{3.7}$$

where χ is an arbitrary variable of interest and N is the number of samples.

4 SENSITIVITY STUDY

This chapter presents a sensitivity study to show the model's sensitivity to the turbulence closure model, sidewall friction coefficient, grid size, and the implemented numerical scheme. All results within the sensitivity study use the idealized inlet configuration and a five centimeter water depth. The parameters were tested and compared in order to determine, to the best of our ability, the model parameters that best represented the laboratory experiments. For the remainder of this thesis, this optimized case is referred to as the base case. The results of the base case are presented in Chapter 4. Seven other cases were run to show the sensitivity of the FREHD model to various parameters before the base case parameters were finalized. These cases are listed in Table 4.1.

Table 4.1: Cases for sensitivity runs for the idealized inlet configuration and 5 cm water depth

Case #	Turbulence model	Sidewall Friction coefficient	dx [cm]	dy [cm]	dz [cm]	Time-steppingl scheme
Base	1 equation	0.005	6.5	6.5	0.5	Euler/Theta
1a	Constant viscosity: 1e-2	0.005	6.5	6.5	0.5	Euler/Theta
1b	Constant viscosity: 1e-6	0.005	6.5	6.5	0.5	Euler/Theta
1c	Constant viscosity: 1e-8	0.005	6.5	6.5	0.5	Euler/Theta
2a	1 equation	0.5	6.5	6.5	0.5	Euler/Theta
2b	1 equation	0	6.5	6.5	0.5	Euler/Theta
3a	1 equation	0.005	2	2	0.5	Euler/Theta
3b	1 equation	0.005	6.5	6.5	0.25	Euler/Theta
4a	1 equation	0.005	6.5	6.5	0.5	Crank-Nicolson
4b	1 equation	0.005	6.5	6.5	0.5	Semi-implicit

Case 1 leaves all parameters the same except for the turbulence closure model. Case

2 adjusts the sidewall friction coefficient between 0 and 0.5. Case 3 adjusts the grid size in both the horizontal and vertical directions. Case 3a tests the effect of reducing the horizontal grid size in both the x and y directions. Case 3b tests the effect of reducing the vertical grid size. Case 4 adjusts the Numerical scheme within the FREHD model. For all cases, only one variable is adjusted between the new case and the base case so that the sensitivity to only one variable can be determined.

4.1 Case 1: Sensitivity to Turbulence Closure Model

The FREHD model was run with two different turbulence closure models and the results will be compared here. The first and simplest turbulence model used assumes that all grid cells have a constant viscosity which can be specified within the model. In cases 1a through 1c, the viscosity in the *x*, *y*, and *z* directions were set equal to three values: 1e-8 $\frac{m^2}{s}$, 1e-6 $\frac{m^2}{s}$, and 1e-2 $\frac{m^2}{s}$ [Table 4.1]. The second turbulence model used is referred to as the one-equation turbulence model and is outlined in the turbulence section of Section 2.2.2.The results using the one-equation turbulence model are presented in Chapter 4. The constant viscosity turbulence model was run first and was determined to be an unfit representation of the laboratory experiments. The results of the model with a constant viscosity turbulence model are presented and compared to the PIV laboratory data.

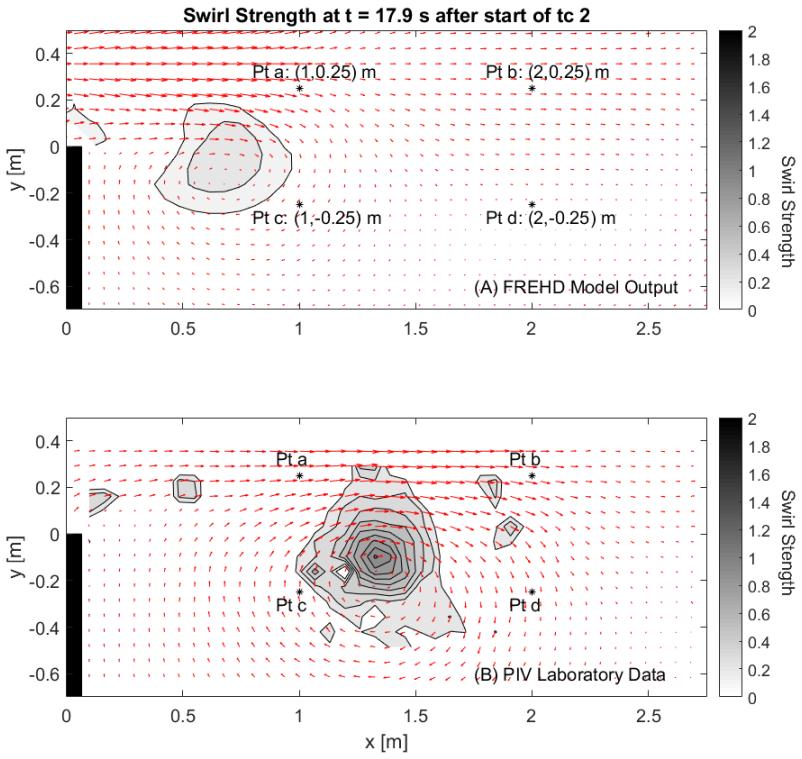

Figure 4.1: Swirl strength for (Top) FREHD model with constant viscosity turbulence model and (Bottom) PIV laboratory data

All constant viscosity turbulence models were able to generate starting jet vortices. Figure 4.1 shows the swirl strength for case 1b vs. the swirl strength in the PIV laboratory data. Although the vortex is present using the constant viscosity model, the vortex location and size are different from the PIV laboratory data. At this time the centroid of the vortex has already traveled approximately 0.5 meters further than the model predicted. The vortex is also about 0.3 meters larger in diameter in the PIV laboratory data than the FREHD model predicts.

The average velocity through the inlet was matched for the PIV laboratory data and

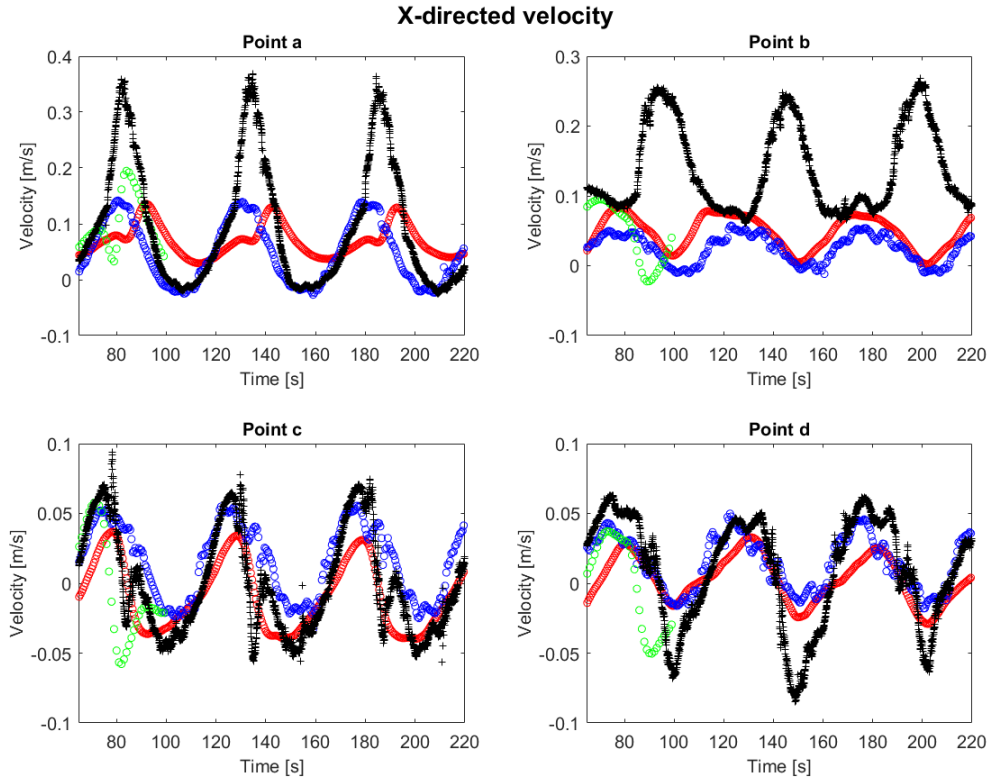

Figure 4.2: X-directed velocity (a) 1 meter away from the inlet and (Bottom) within the inlet for case 1 (Blue) and the base case (Red)

the FREHD model runs. No attempt was made to match the velocities at any other points throughout the domain. Figure 4.2 shows the velocities for cases 1a through 1c at four other points throughout the domain. Point a is located within the jet and one meter downstream of the inlet. In an x,y coordinate system the point is located at (1,0.25) meters [Figure 4.1]. The magnitude of the peaks at point a have a relative error of approximately 65% for cases 1a and 1c. The relative error for case 1b is slightly less. The magnitude of the peaks in case 1b are approximately 46% lower than the PIV laboraty data shows. At point b, the mignitudes of the velocities for all three cases show different behavior than the PIV laboratory data. For all three constant viscosity cases, the x velocity at point b oscillates

around 0 whereas the PIV laboratory data remains positive throughout the entire time series. The flow in the PIV data at 2 meters downstream of the inlet is never fully effected by the reverse tide. The velocities slow down during this time but never change directions. The constant viscosity models are unable to predict this behavior. The oscillation around 0 shows that the flow is predicted to change direction with every reverse tide at 2 meters downstream of the inlet.

There is also a phase difference between the constant viscosity model runs and the PIV laboratory data. Within the inlet there is good phase agreement between the model and the PIV data for all three cases. Case 1b shows an 8 seconds phase difference at point a. The model reaches its peak after the PIV laboratory data. This phase lag grows at point b to approximately 20 seconds or 40% of the tidal period. Case 1a shows a phase difference in the opposite direction. The model reaches a peak approximately 2-3 seconds before the PIV laboratory data. This phase lag also grows at point b and is similar to the phase lag in case 1b.

All three constant viscosity cases show some similar behaviors when comparing vortex properties to the PIV laboratory data. The total circulation in the primary vortex reaches a maximum of 0.11 $\frac{m^2}{s}$ for all three cases. This gives a relative error of 73% when compared to the PIV laboratory data [Figure 4.3c]. The centroid location of the vortices is consistently closer to the inlet for all three cases. The location of the centroid of the vortex is not known beyond the PIV field of view [Figure 4.3a; dashed line], but the vortices propagated up until or beyond 2.74 meters. The vortices in the constant viscosity cases

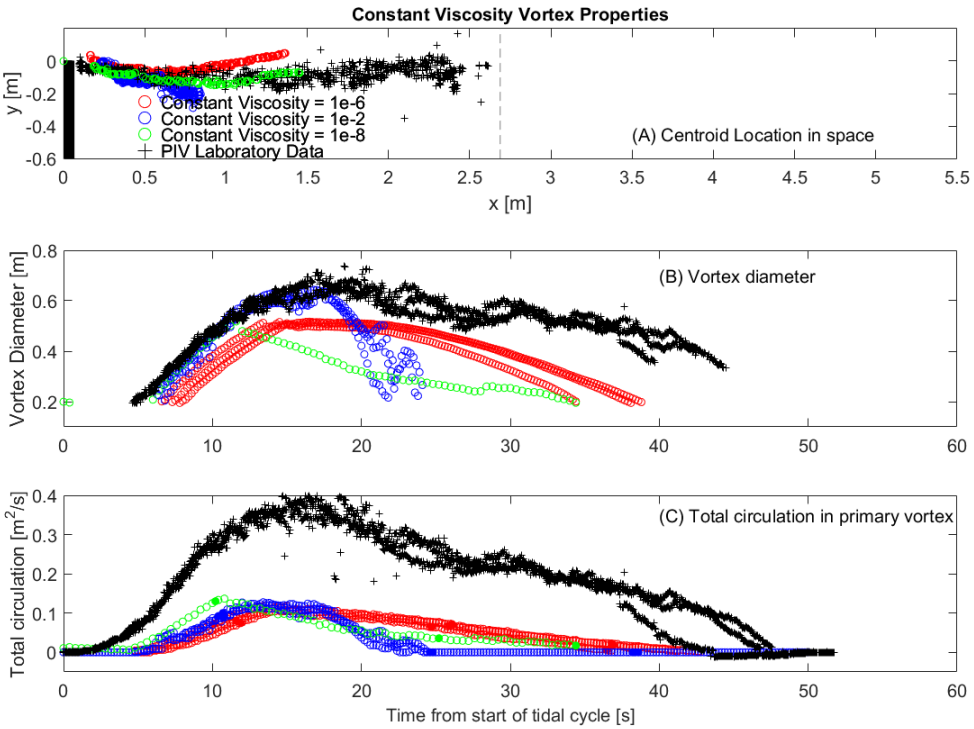

Figure 4.3: (A) Vortex centroid location, (B) vortex diameter, and (C) Total circulation within the primary vortex for constant viscosity FREHD model and PIV laboratory data.

only propagated a maximum distace of 0.85, 1.5, and 1.4 meters respectively for cases 1a through 1c. Case 1a showed the vortices dissipating the fastest, most likely because the relatively high viscosity dampened the flow. Case 1b and 1c showed similar propagation distances [Figure 4.3a].

The vortex diameters varied between the three constant viscosity cases. Case 1a showed the largest vortices. This is reasonable because the high viscosity does not allow for a tight vortex to form so more fluid is entrapped in the vortex allowing for larger diameters. The dampened flow due to the high viscosity shows the vortex dissipating completely by about halfway through the tidal cycle or 25 seconds. Case 1b shows a similar shape to the

PIV laboratory data but consistently underestimates the vortex diameter. This behavior is also seen in Figure 4.1. Case 1c matches the PIV data for the first 10 seconds of the tidal cycle and then the vortices are much smaller than both the PIV laboratory data and the vortices seen in the other two cases. The low viscosity in case 1c allows for a very tight vortex to form so it is reasonable that the diameters would be smallest for this case.

Overall, the constant viscosity turbulence model is not a good representation of the flow field even though it is able to generate primary starting-jet vortices. There is no constant viscosity value that is able to correctly capture the vortex behavior seen in the laboratory. The vortices in all three cases do not propagate far enough or have nearly enough circulation to behave in a similar way.

The results presented in this section show that a more advanced turbulence model is required to capture the trajectory of the starting-jet vortices with tidal flow through an inlet. Multiple turbulence models were investigated but the one-equation turbulence model outlined in Section 2.2.2 was chosen as the best fit to the data for the current model setup. These results are presented in Chapter 4.

4.2 Case 2: Sensitivity to Sidewall Friction Coefficient

The sidewall friction coefficient quantifies the amount of friction present along the wall of the inlet. Although the bottom friction coefficient was able to be calculated with relative certainty, there is no reasonable way of analytically calculating the correct side-wall friction coefficient. Three FREHD model runs were used to test the sensitivity to the

sidewall friction coefficient. The first run used in the study is the base case. Cases 2a and 2b used identical parameters to the base case except the sidewall friction coefficients were changed to 0.5 and 0 respectively to test the sidewall friction coefficient sensitivity [Table 4.1].

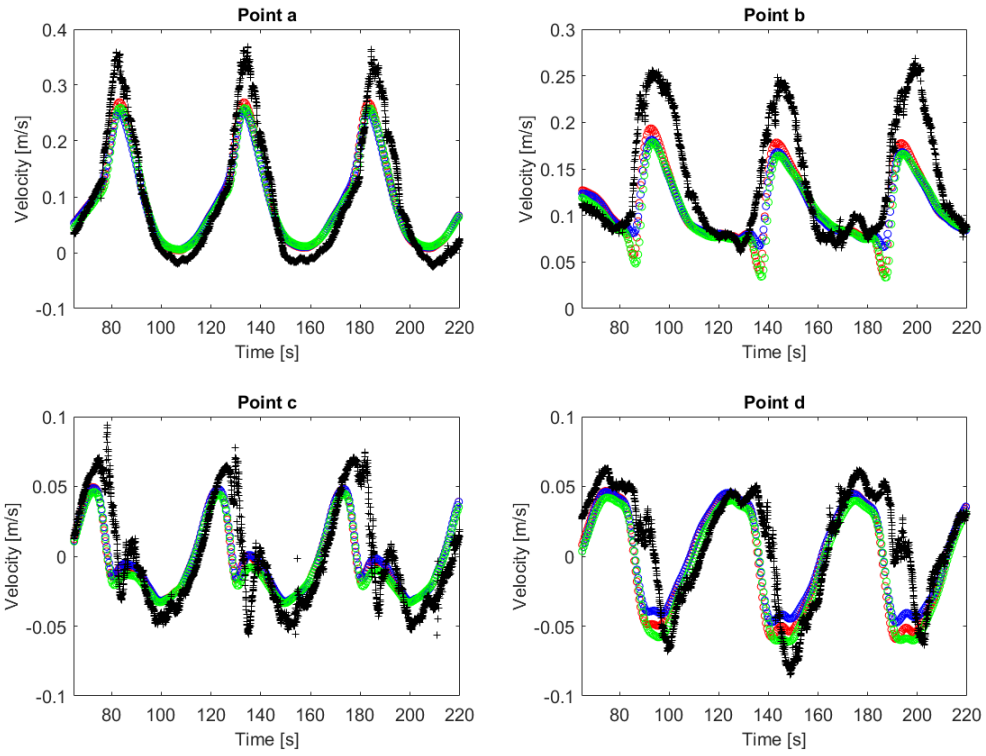

Figure 4.4: X-directed velocities at points a-d for PIV laboratory data and model runs with sidewall friction coefficients of 0, 0.005, and 0.5

The x-directed velocities are similar for all three sidewall friction coefficient values [Figure 4.4]. The shapes at all four points do not change when the sidewall friction is varied. The only slight difference between the cases is the peak and trough values. At point a and c, the velocities are the greatest for the base case and are slightly lower for cases 2a and 2b [Figure 4.4a;c]. At point d, the values at the troughs vary slightly when the

sidewall friction coefficient is changed. The most negative velocities are predicted with a sidewall friction coefficient of 0.5 followed by 0.005 and finally, 0, which shows the least negative velocities in the troughs at point d [Figure 4.4a;c].

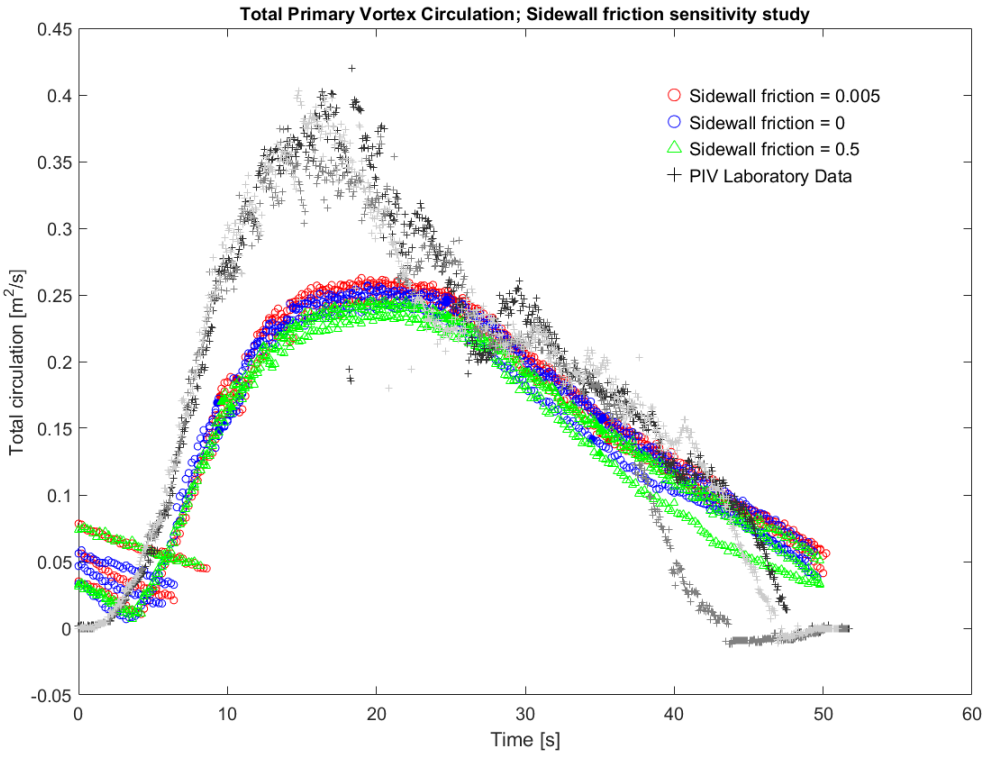

Figure 4.5: Total circulation within the primary vortex for PIV laboratory data and model outputs with sidewall friction coefficients of 0, 0.005, and 0.5

The total circulation within the primary vortex for the base case, case 2a, and case 2b are all similar. The maximum values only vary by approximately 0.01 $\frac{m^2}{s}$. The base case predicted the highest total circulation with a maximum value of about 0.25 $\frac{m^2}{s}$. Case 2a predicted slightly less total circulation within the primary vortex followed by case 2b which predicted the lowest values [Figure 4.5]. The base case has some friction along the inlet wall which creates higher velocity gradients at the boundary than the zero-friction case and therefore increases the amount of total circulation. These increased velocity gradients at the boundary allow for more circulation in the base case than the free slip boundary condition.

This is only true for small friction values. When the friction coefficient increases to 0.5, the sidewall friction dampens the flow and no longer aids in circulation production.

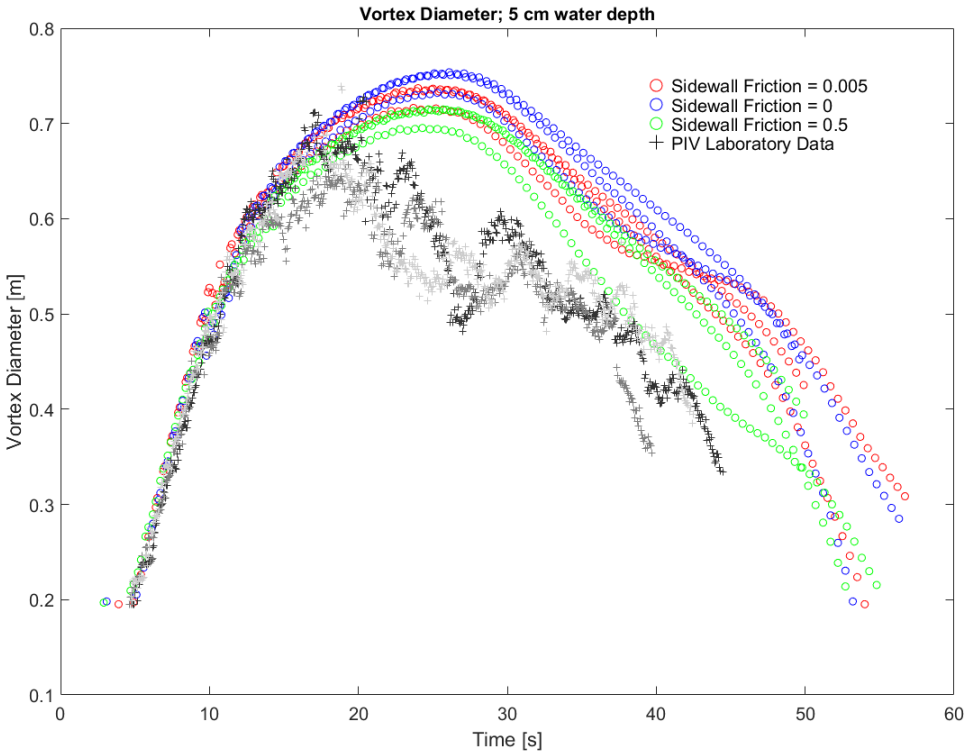

Figure 4.6: Primary vortex diameter for PIV lavboratory data and model outputs with sidewall friction coefficients of 0, 0.005, and 0.5

The diameter of the primary vortex decreases with increasing sidewall friction coefficients. The largest vortices are predicted when the boundary is free slip and the smallest vortices are predicted when the sidewall friction coefficient is at a maximum of 0.5. All three model runs reach a peak at approximately the same time after the start of the tidal cycle and decrease at similar rates since the slope after the peak is approximately the same [Figure 4.6].

Overall, the sidewall friction coefficient has a small effect on model performance.

The laboratory setup suggests that the sidewall friction value must be present since the laboratory setup did not attempt to eliminate the friction on the inlet walls. In the laboratory, the inlet was constructed of PVC pipe which is a relatively smooth material; therefore, the frictional effects should be small. A sidewall friction coefficient of 0.005 was chosen as the best case because it allows for some frictional effects without allowing friction to dominate.

4.3 Case 3: Sensitivity to Model Grid Size

The grid size is a key component to how the model performs. A smaller grid size can allow for more resolved details within a flow but often increases the computational time tremendously. The grid size chosen as the base case for the FREHD model was 6.5x6.5 cm in the x and y directions and 0.5 cm in the z direction. This allows for 12 grid cells across the inlet width. In case 3a, the grid size was reduced in the horizontal direction with a constant vertical layer thickness of 0.5 cm. This is important when considering the formation of secondary vortices. The secondary vortices seen in the laboratory data have a maximum diameter of 7-8 cm. In order to capture a vortex, it is ideal to have approximately 8 to 10 grid cells over the length of the vortex. For the FREHD model with a uniform, structured grid this would require too much computational time to run. A grid size of 2x2 cm was the smallest grid size possible with a reasonable computational time so this was used to test the convergence of the vortex features with grid size reduction.

It is expected that as the grid size decreases, the vortex characteristics which rely on spatial derivatives will increase. Higher swirl strength and vorticity values were expected

with a smaller grid size. This section emphasizes the convergence of vortex characteristics such as vortex size, location, and total circulation.

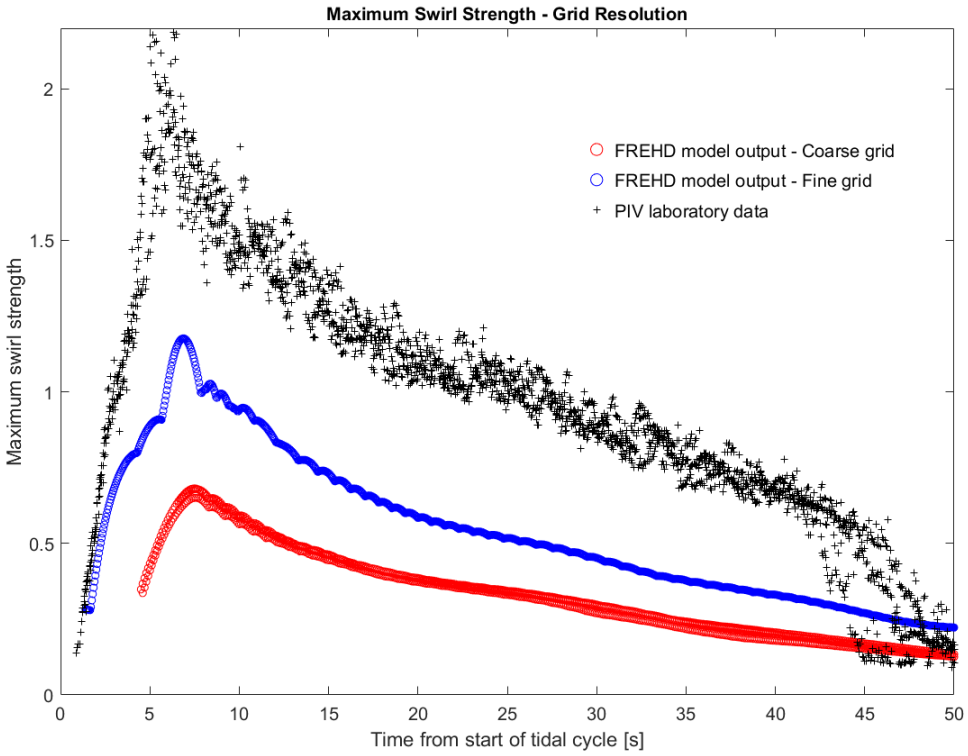

Figure 4.7: Maximum swirl strength for fine and coarse grid FREHD model run and PIV laboratory data

As expected, decreasing the grid size within the model increased the maximum swirl strength values predicted by the model [Figure 4.7]. In the coarse grid model run the swirl strength reached a maximum of 0.7 $\frac{1}{s}$ and the fine grid model run reached a maximum of 1.2 $\frac{1}{s}$. Neither of the model runs were able to get the high swirl strength values shown in the PIV laboratory data. Both model runs reach a maximum swirl strength value approximately 8 seconds after the start of the tidal cycle. This agrees well with the timing of the PIV laboratory data [Figure 4.7].

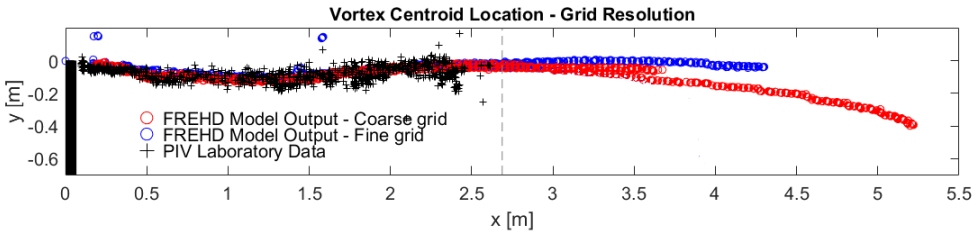

Figure 4.8: Location of vortex centroid for fine and coarse grid resolution model run and the PIV laboratory data

Although the maximum swirl strength does not converge as the resolution is increased, the location of the vortex centroid has a similar trajectory to the observations for both the fine and coarse grid model. After the end of the PIV field of view, the fine and coarse grid model runs both show a relatively straight trajectory until the vortex eventually dies out [Figure 4.8]. The coarse grid showed vortices propagating between 3.7 and 5.2 meters from the inlet depending on the tidal cycle. The fine grid model was only run for two tidal cycles but the model showed the vortex dying out about 4.4 meters from the inlet which is within the range of distances from the coarse grid model.

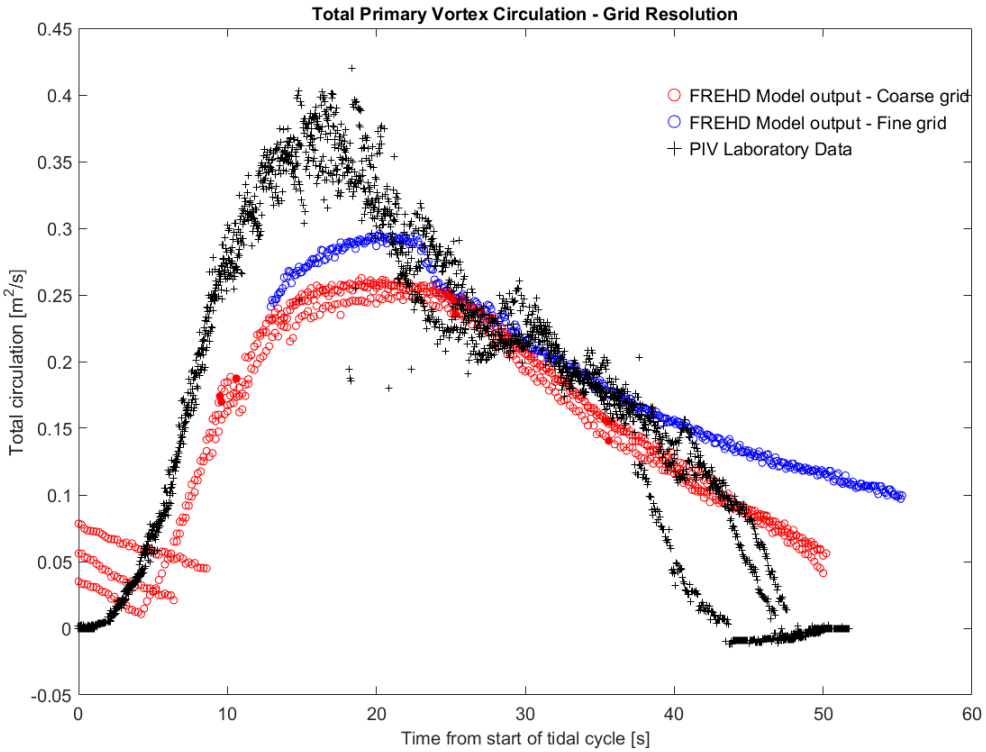

Figure 4.9: Total circulation within the primary vortex for fine and coarse grid resolution model runs and the PIV laboratory data

The fine and coarse grid model runs predicted a difference in total circulation within the primary vortex of about 0.25 $\frac{m^2}{s}$ at the peak [Figure **??**]. The increase in circulation is most likely due to the higher vorticity values within the center of the vortex. The total circulation within the primary vortex over time has a similar shape for the coarse and fine grid model runs. They both agree well with the PIV laboratory data beginning about halfway through the tidal cycle. Before this point, the total circulation is under predicted for both the coarse and fine grid model runs [Figure 4.9].

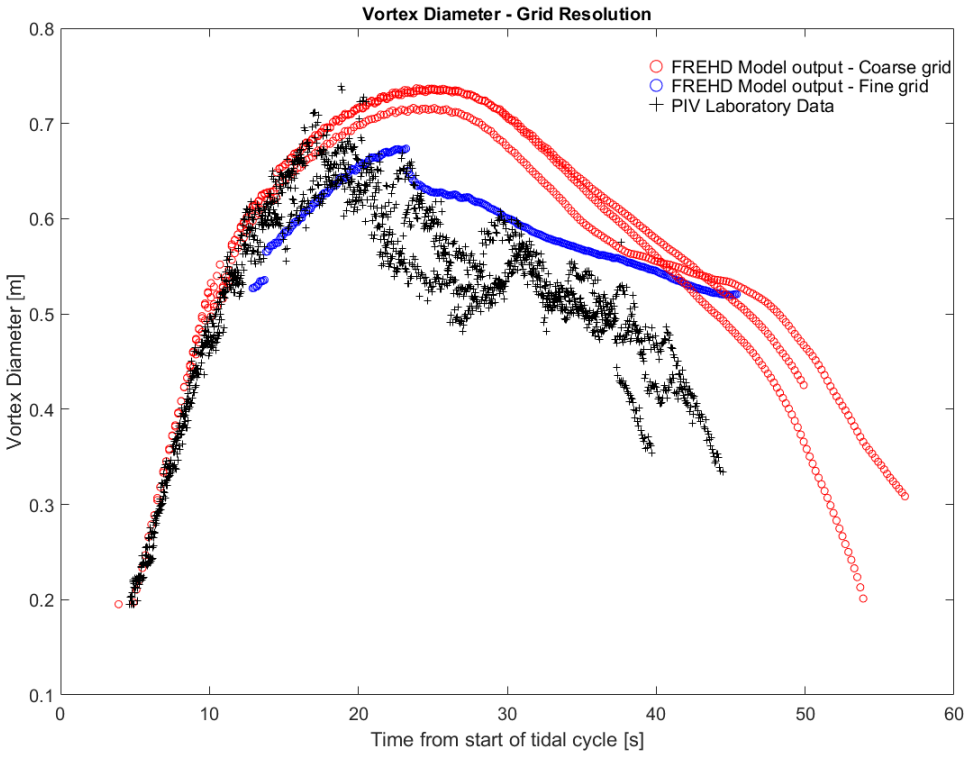

Figure 4.10: Primary vortex diameter for fine and coarse grid resolution model runs and the PIV laboratory data

The shape of the diameter of the primary vortex over time agrees better for the fine grid model run than for the coarse grid model run [Figure 4.10]. The fine grid model predicts a sharp peak and then levels off until the end of the tidal cycle. This is also seen in the PIV laboratory data although the PIV laboratory data hits a peak about 5 seconds before the model predicts. The location of the peak is similar between the fine and coarse grid model runs although it deviates from the PIV laboratory data. The vortex diameter in the fine grid model run is consistently larger in the model than the PIV laboratory data. This is also the case for the coarse grid model run.

Overall, the vortex properties such as size and trajectory converge as the grid size is decreased such that the 6.5x6.5 cm case is considered adequate to draw conclusions about the vortex behavior moving forward.

4.4 Case 4: Sensitivity to Time-Stepping Scheme

The FREHD model uses a predictor/corrector scheme to arrive at a result at each time step. This scheme can be altered by changing a single coefficient within the input files to FREHD. Three options were used to test the sensitivity of the model to the scheme chosen. The first, the base case, uses the predictor corrector method with an initial Backwards-Euler method followed by a corrector step with a theta-method that has a time n and $n+1$ weighting of 0.4 and 0.6. The second scheme, case 4a, uses a corrector step with a Crank-Nicolson method that has a time n and $n+1$ weighting of 0.5 and 0.5. Overall the theta-method is only slightly dissipative compared to the Crank-Nicolson method in most cases. The third scheme tests the model with an initial theta method but no corrector step. This is case 4b in Table 4.1.

when different predictor/corrector schemes are used within the FREHD model, the centroid location follows the same trajectory as the vortex propagates away from the inlet. The semi-implicit method shows the vortex travelling the shortest distance away from the inlet compared to the other two cases. The theta and Crank-Nicolson methods show the vortices propagating about 0.5 meters further than the semi-implicit method [Figure 4.11(A)]. The maximum diameter of the primary vortex varies between 0.75 $\frac{m}{s}$ and 0.79 $\frac{m}{s}$. The semi-

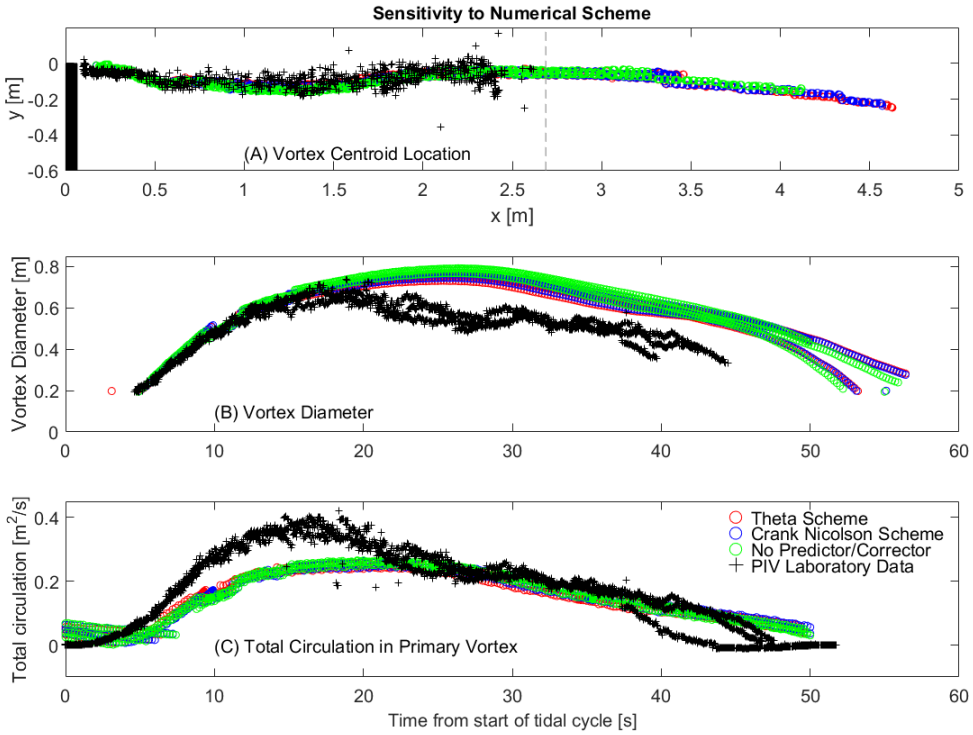

Figure 4.11: Vortex properties including (A) vortex centroid location, (B) primary vortex diameter, and (C) total circulation within the primary vortex using various numerical schemes

implicit method predicts the largest diameter followed by the Crank-Nicolson method and finally the theta method [Figure 4.11(B)]. The maximum total circulation varies between 0.257 and 0.265 $\frac{m^2}{s}$ and the shape is the same for all three cases [Figure 4.11(C)].

4.5 Summary

The base case represents the laboratory setup to the best of the FREHD model's ability. The turbulence closure model has a large impact on how the model performs. The one-equation turbulence model provides the best agreement to the laboratory data. More

turbulence closure models are discussed in Section 5.3. The sidewall friction only slightly changes the model results when varied between 0 and 0.5. We believe that 0.005 is a good representation of the laboratory setup. The horizontal grid resolution creates larger swirl strength values, which approach the values seen in the PIV data.We believe we have achieved convergence and that the coarse grid resolution is adequate to measure model performance. The fine grid would be preferred to use for the base case but due to time constraints, that was not possible. Finally, similar results were produced for all three time-stepping schemes tested.

5 FREHD RESULTS

The following sections discuss the accuracy of the FREHD model when compared to the PIV laboratory data for tidal cycles two through four. This thesis does not discuss the first of the four tidal cycles since the first tidal cycle shows different behavior since the domain is originally at rest. The FREHD model was run with varying input parameters for the idealized inlet configuration with a five centimeter water depth. The input parameters with the best fit to the data are presented in section 2.2.2. In this chapter, the model results for the model run with the best fit input parameters, idealized inlet configuration, and five centimeter water depth are presented first. Next, the results are presented for the other two water depths with an idealized inlet configuration starting with the three centimeter water depth, and followed by the nine centimeter water depth. Lastly, the results for the large barrier island and long jetty cases are presented.

5.1 Idealized Inlet Configuration

The average velocity through the inlet was determined from the PIV data for each of the laboratory experiments. This was the key metric which was matched for each model run by adjusting the boundary conditions and model parameters. All parameters within the model remained constant as the model inflow was adjusted until the average velocity through the inlet for the model and the PIV data agreed. The inflow values with the best agreement are shown in Table 2.1.

5.1.1 Five Centimeter Water Depth - Base Case

For the 5 cm case, the peak velocity and phase across the inlet channel match the PIV laboratory data well. The shape of the velocity profile from the peaks to the troughs and vice versa is also mirrored well in the model output [Figure 5.1]. Peak velocities are underpredicted by 17.6% on ebb tide while peak velocities on flood tide were predicted within 4.7% relative error. The phase error at the fourth tidal cycle is 7.8% of the tidal period. This is partly due to the fact that the tide was reversed manually in the lab, with inconsistencies of a few seconds. Overall, the model agreement with the measured forcing through the channel is acceptable, leading to errors less than 20%.

The largest vortex that forms within the laboratory data is called the primary starting-jet vortex. The FREHD model was able to resolve the primary vortices that form with tidal flow through an inlet. In both the model and laboratory data, the vortex spins up at the inlet mouth and then eventually detaches and begins to propagate away from the inlet. The swirl strength once the vortex has detached from the inlet mouth is shown for both the FREHD model and the PIV laboratory data together with velocity vectors on the model grid [Figure 5.2]. The swirl strength was used to extract vortex characteristics from the velocity fields for the model and laboratory data.

In the laboratory data, smaller secondary vortices also form in addition to the primary starting-jet vortex [Figure 5.2b e.g. at the point (0.5,0.2) m]. These tend to detach from the inlet and then begin propogating around the primary starting-jet vortex (see swirl strength patches at x=2m). The model was unable to resolve these secondary vortices, most

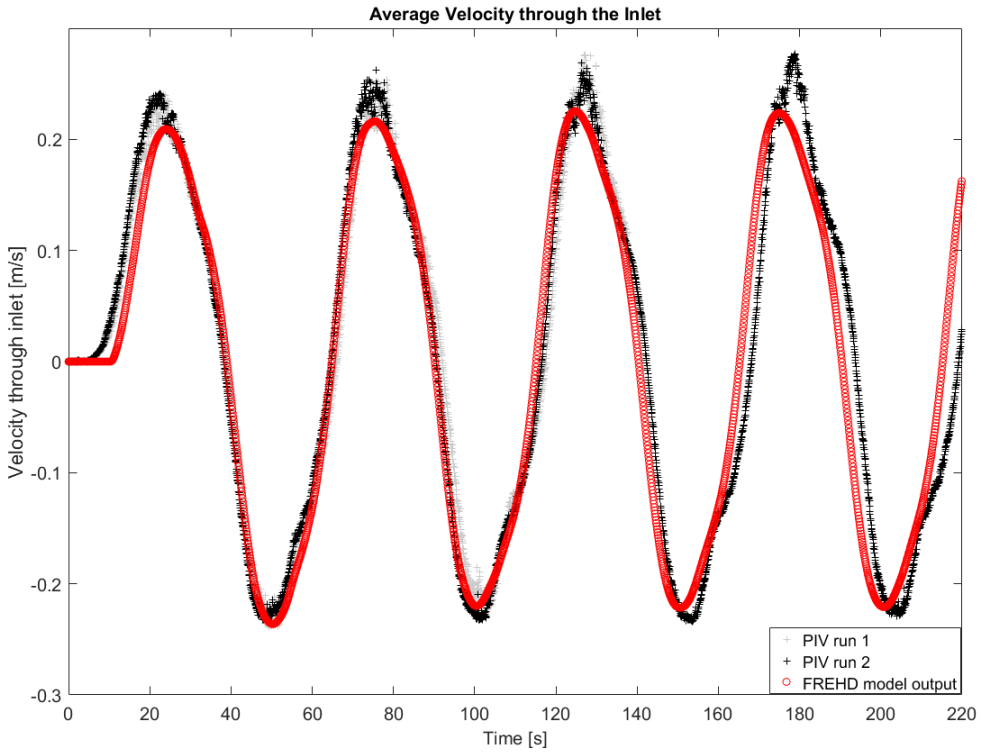

Figure 5.1: Average Velocity through the inlet for idealized inlet configuration with five centimeter water depth

likely because of resolution constraints or numerical dissipation within the model. These secondary vortices shed with a frequency that matches a Strouhal number of 0.2. These vortices are interpreted to be vortices shed by boundary layer separation from the sharp edge of the inlet. The model is only capable of relatively coarse resolution compared to the boundary layer thickness so it is unlikely that the model will be able to resolve these secondary vortices with the present numerical scheme.

The *u* and *v* components of the velocities for tidal cycles two through four at points a-d (see fig. 5.2) throughout the domain are shown in Figures 5.3 and 5.4. Points a and b are within the jet at approximately one third of the inlet width and at 1 and 2 meter distances

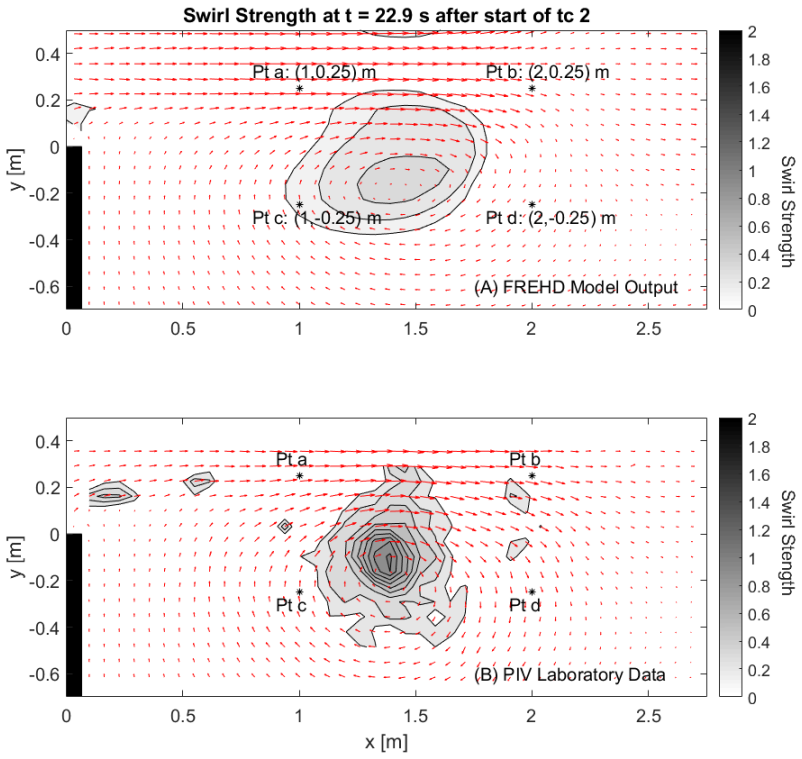

Figure 5.2: Swirl strength comparison for idealized inlet configuration and 5 cm water depth

from the inlet respectively. Points c and d are located behind the inlet, also at 1 and 2 meter distances respectively [Figure 5.2]. The velocity through the inlet was matched as a model calibration parameter but no other attempt was made to match the velocities at any other points. In general, the magnitude of the peak velocities is higher for the laboratory data than the model but the model results are in phase with the laboratory data without any adjustment. The root mean square (rms) errors for both u and v components of the velocity range from 0.02 to 0.05 $\frac{m}{s}$. The x-directed velocity has a maximum rms error of 0.0466 $\frac{m}{s}$ at point b and a minimum of 0.025 $\frac{m}{s}$ at point c. The rms error for the v component of the velocity has a maximum of 0.041 $\frac{m}{s}$ at point c and a minimum of 0.0194 $\frac{m}{s}$ at point a

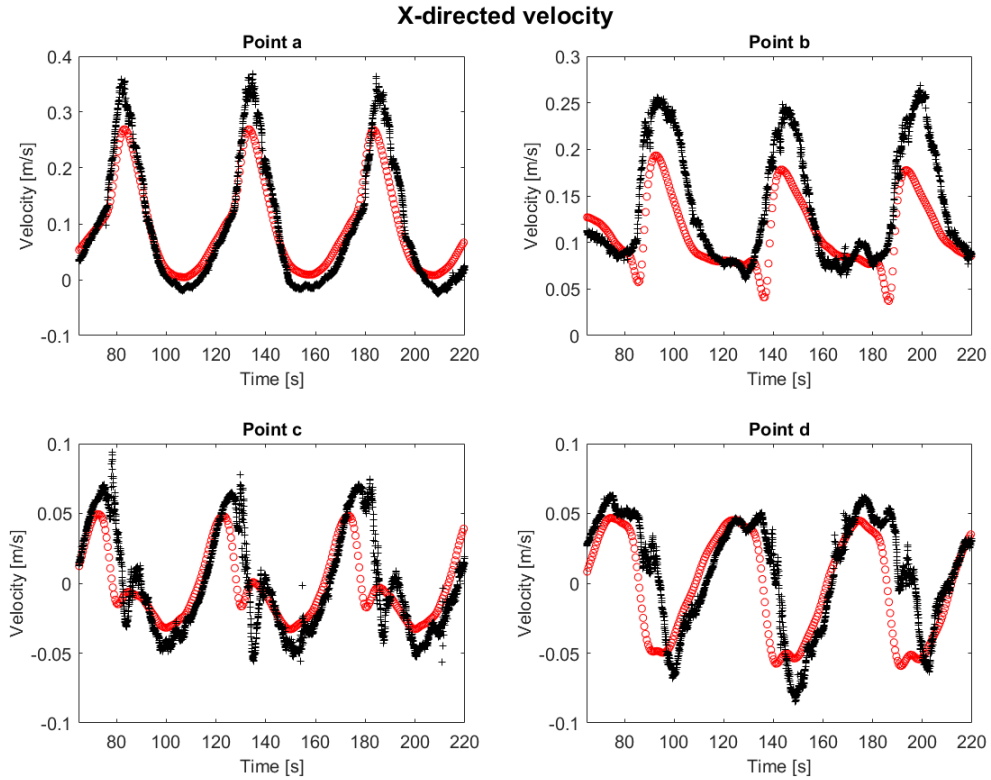

Figure 5.3: X-directed velocities at points a-d for FREHD model and laboratory PIV data.

[Table 5.1].

Table 5.1: RMS Error for idealized inlet configuration with 5 cm water depth

Point	u component rms error $[\frac{m}{s}]$	v component rms error $[\frac{m}{s}]$
a	0.0383	0.0194
b	0.0466	0.02
c	0.025	0.041
d	0.0299	0.0314

The mean, standard deviation, skewness, and kurtosis were calculated for u and v at points a through d for both the model and laboratory results and are shown in Table 5.2 and 5.3. At point a, the mean x-directed velocity from the FREHD model is within 4% of the PIV laboratory data. The standard deviation is higher for the laboratory data

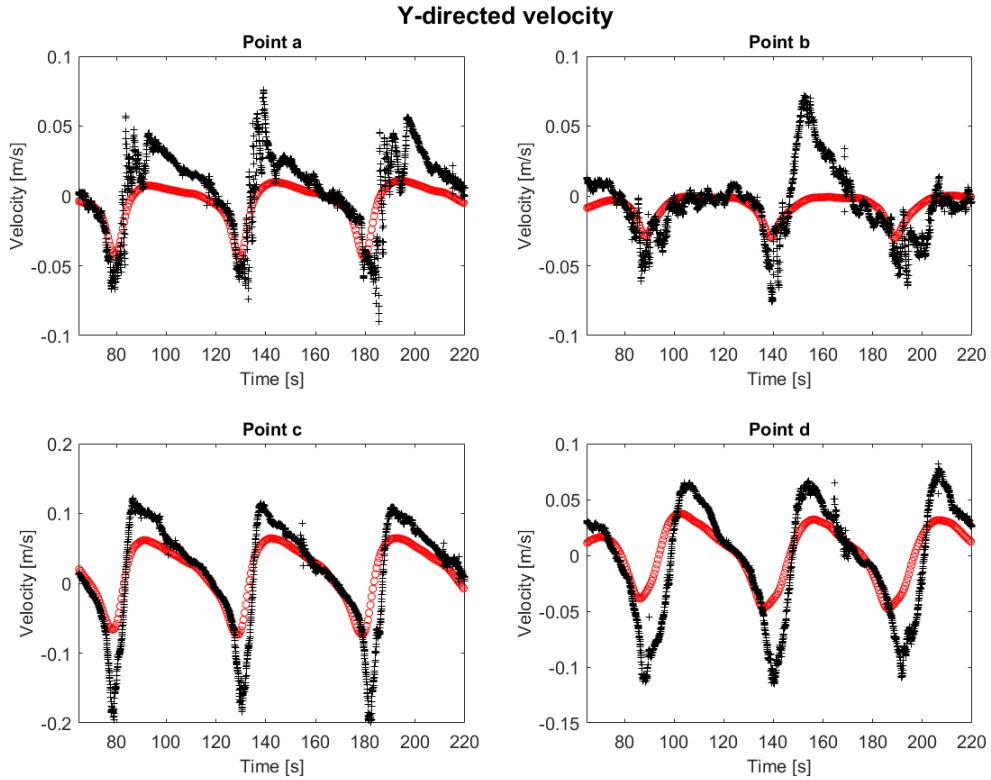

Figure 5.4: Y-directed velocities at points a-d for FREHD model and laboratory PIV data.

than the model as expected due to noise in the laboratory experiments, turbulence, and the existence of secondary vortices. The skewness and kurtosis agree well with values within 5% of eachother between the model and measurement. The phase agreement is quantified by comparing the time from peak-to-peak and from valley-to-valley. At point a, the time between peaks and valleys is almost identical to the tidal period, T, of 50 s. The time between peaks agree within 2.75 s or 5.5% of the tidal period. The time between valleys agree within 5 s or about 10% of the tidal period. At point b, which is located within the jet but further from the inlet, the deviations at the peaks appear to grow. The mean x velocity at point b is greater for the laboratory data than the model predicts, but the fluctuations

remain in phase. The time between peaks agrees within 4 s or 8% of the tidal period, and the time between valleys agrees within 1.1 s or 2.2% of the tidal period.

At point c, the mean x-directed velocity is approximately 0 for both the model and laboratory data. The standard deviation is higher for the laboratory data than for the model, as expected. The time between peaks agrees within 1.2 s or about 2.4% of the tidal period and the time between valleys agrees within 2.2 s or about 4.4% of the tidal period. The overall shape of the velocity at point c emphasizes the power of the FREHD model. The model is able to capture a double peaked trough within the velocity time series at this location that also occurred in the laboratory data [Figure 5.3c]. Skewness and kurtosis are also similar between the model and the data, with differences ranging from 3 to 25% relative error.

Table 5.2: Bulk statistics of u velocity component at points a through d

Point		Mean	Std	Skewness	Kurtosis
a	FREHD model	0.0733	0.1223	0.4294	1.7508
	laboratory data	0.075	0.1462	0.5862	1.9829
b	FREHD model	0.164	0.0523	1.052	2.757
	laboratory data	0.1263	0.0832	0.8447	2.1964
c	FREHD model	-0.0089	0.0213	0.3011	2.0218
	laboratory data	-0.0115	0.0288	0.2656	2.107
d	FREHD model	-0.0016	0.0311	0.3781	1.5713
	laboratory data	0.0043	0.0402	0.0595	1.5224

The y-directed velocities over time show similar trends to the x-directed velocities. The y velocities predicted by the model are generally lower than the velocities observed in the laboratory data but the phase is similar as discussed above. At points a and b, located in the jet, the laboratory data shows much more noise in the y velocities. The model results,

Table 5.3: Bulk statistics of v velocity component at points a through d

Point		Mean	Std	Skewness	Kurtosis
a	FREHD model	-0.000936	0.0186	-1.0031	3.0179
	laboratory data	0.0144	0.0263	-0.7659	3.579
b	FREHD model	-0.006	0.0109	-1.5361	4.2851
	laboratory data	-0.0011	0.0242	-0.629	3.5029
c	FREHD model	0.0317	0.0419	-1.0556	2.7556
	laboratory data	0.0402	0.0737	-1.3058	4.4788
d	FREHD model	0.0075	0.0332	-0.6633	2.2456
	laboratory data	0.0083	0.0634	-0.6427	2.5846

however, are smooth as expected since all of the turbulence effects and secondary vortices are not included in the model. At points c and d, the model does a better job of predicting the positive velocities than the negative ones since the velocity gradients for the negative values shown in the laboratory data are much sharper than the velocity gradients for the positive values.

Figure 5.4a shows fluctuations in the PIV laboratory data when the vertical velocity first becomes positive within each tidal cycle. These fluctuations are not predicted by the model. These fluctuations could potentially be explained by the secondary vortices. As the secondary vortices pass this point, they cause the vertical velocity to oscillate with each new vortex that passes. These fluctuations are only seen at point a, which strengthens the claim that they are caused by the secondary vortices since point a is the only location that would experience the effects of secondary vortices. This would explain why these fluctuations are not predicted by the model since the model is unable to capture the secondary vortex formation.

The velocities within the domain are a good way to analyze the flow field. The vortex

characteristics within the flow field can be better understood by analyzing the vortex size, location, and total circulation.

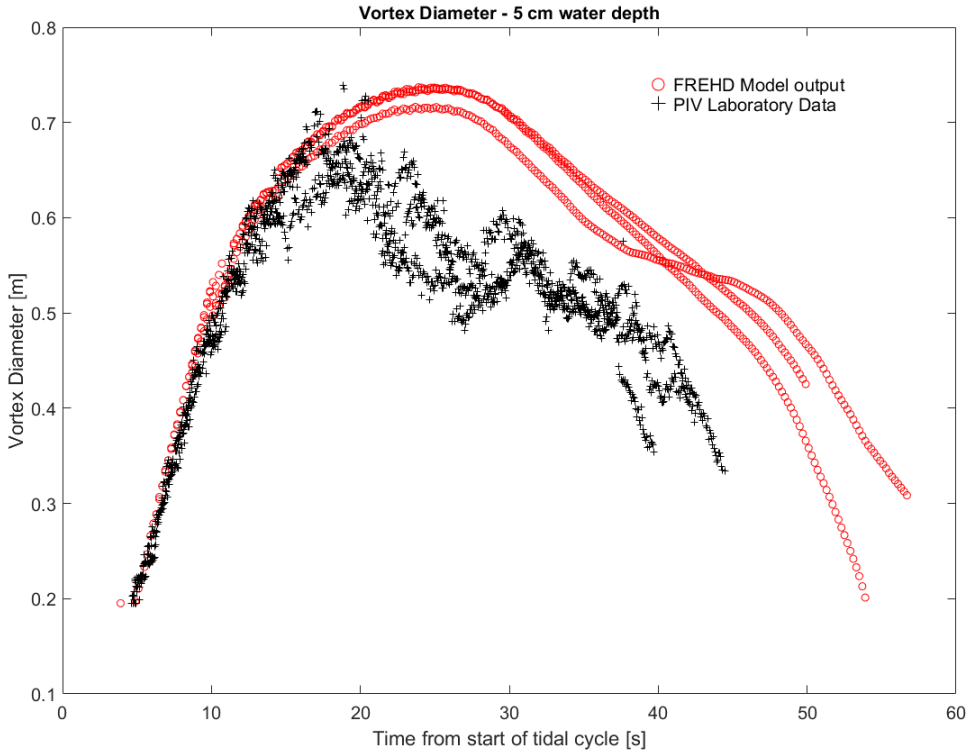

Figure 5.5: Vortex diameter for idealized configuration with 5 cm water depth.

The model predicts larger vortices than were observed in the laboratory data. The maximum diameter of the vortices in the model was about 0.72 m whereas the laboratory data showed a maximum around 0.7 m. Although this agreement is close, the model over-predicts the vortex size throughout the second half of the tidal cycle, with errors of about 25%. The vortex within the model reached a peak diameter about 25 s from the start of the tidal cycle. This was approximately 8 s later than the laboratory data, which showed a peak 17 s after the start of the tidal cycle [Figure 5.5]. In both the model and laboratory

results, the vortex size levels off after it reaches its peak and before beginning to decrease in size again.

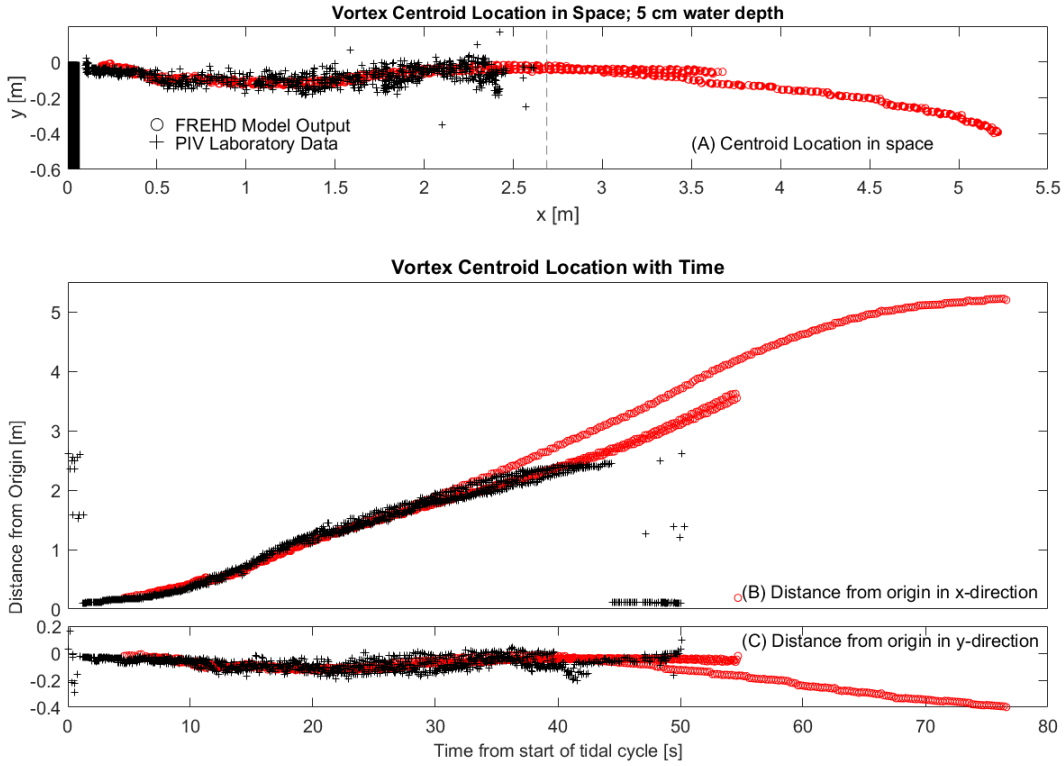

Figure 5.6: Vortex centroid variation in (A) space and (B,C) time for idealized configuration with 5 cm water depth.

The vortex centroid was calculated for both the model and laboratory results. The location of the centroid in space follows the same trajectory for both the model and laboratory data [Figure 5.6a]. There is a slight curve in the vortex trajectory, which is mimicked in the model. The trajectory after the end of the PIV field of view cannot be verified for the model since there is no laboratory data past this location. This new information predicted by the model could be helpful in determining the long term trajectory of starting jet vortices over their entire lifespan. The centroid location over time is also similar between the

model and laboratory results. This proves that the vortices are moving at similar speeds in both cases [Figure 5.6b,c].

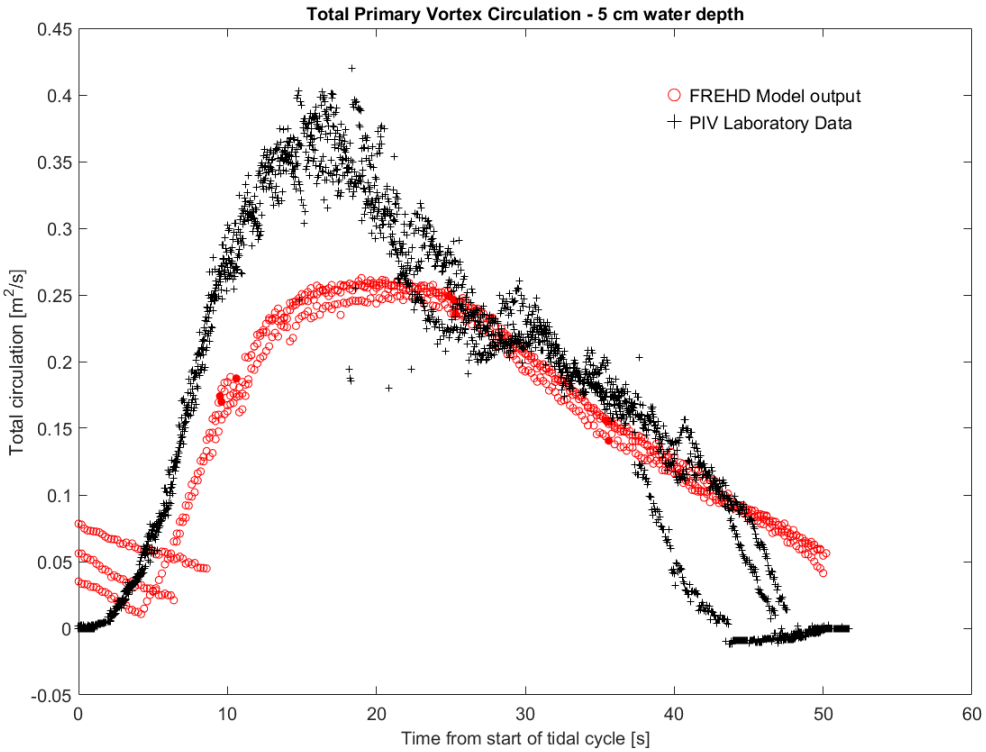

Figure 5.7: Total circulation within the primary vortex for idealized configuration and 5 cm water depth.

The total circulation within the primary vortex was calculated according to the vorticity and circulation described in section 3.1.2. The peak circulation in the primary vortex for the laboratory data is about 0.4 $\frac{m^2}{s}$. The model predicts a maximum total circulation within the primary vortex of 0.25 $\frac{m^2}{s}$. About halfway through the tidal cycle, the total circulation predicted by the model agrees well with the total circulation observed from the laboratory data but between 10 and 25 s after the start of the tidal cycle, the model is under predicting the total circulation within the primary vortex [Figure 5.7]. It is hypothesized

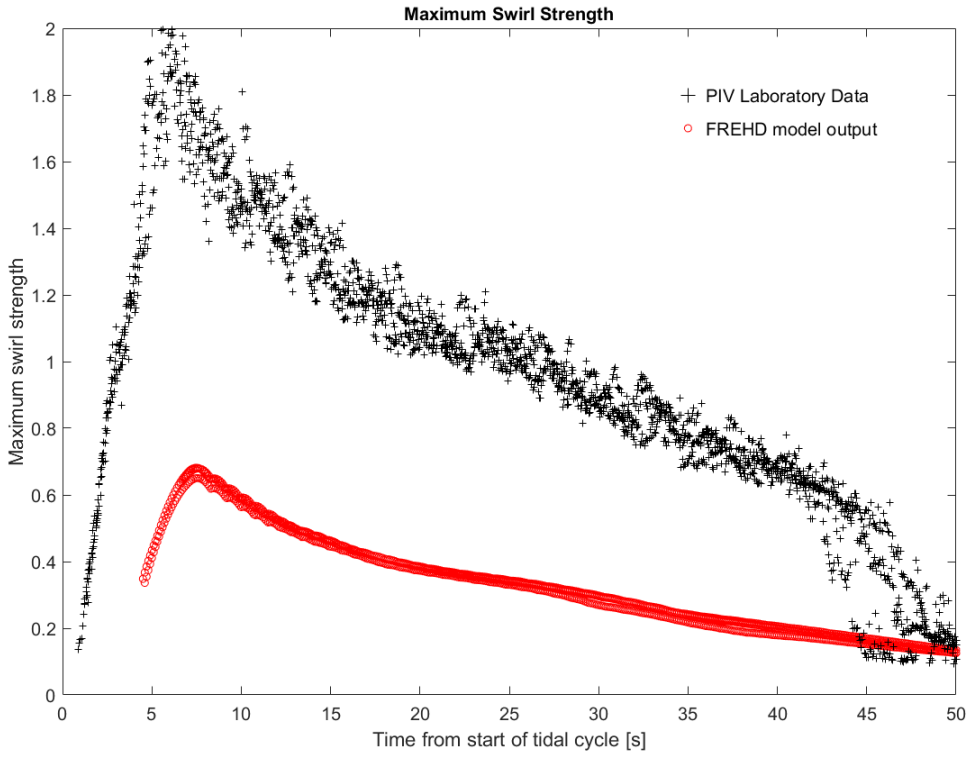

Figure 5.8: Maximum swirl strength within the primary vortex.

that the model is missing this circulation because it is only able to resolve the primary vortex. In the PIV laboratory data, secondary vortices are observed to form at the inlet mouth and then rotate around the primary vortex [Figure 5.2b]. They eventually merge with the primary vortex contributing to the total circulation. These secondary vortices form and join the primary vortex between 10 and 25 s from the start of the tidal cycle. Since the model does not resolve the secondary vortices, their input of circulation is not captured in the model results. It may also be that numerical dissipation prevents the model from reaching the high, observed vorticities in the center of the vortex.

The maximum swirl strength within the primary vortex is underestimated by the

model [Figure 5.8] throughout the tidal cycle. Physically, this means the period of rotation for the model vortex is longer than the measured rotation rates. The shape of the maximum swirl strength over time is similar for both the laboratory data and the model. The maximum swirl strength reaches a peak approximately 7-8 s after the start of the tidal cycle and then slowly decreases throughout the rest of the tidal cycle. The laboratory data shows a maximum swirl strength value within the primary vortex of approximately 2 $\frac{1}{s}$; whereas, the model only predicts a maximum swirl strength value of about 0.7 $\frac{1}{s}$. These large swirl strength values occur over very small spatial scales so most likely the model is unable to capture these values due to the relatively coarse grid size. This is discussed further in section 3.2.3. Although the maximum swirl strength values in the model are too low, it does not affect the other vortex properties to the same degree.

5.1.2 Three Centimeter Water Depth

The knowledge gained from the calibration of the model for the five centimeter water depth was carried over and applied to the three centimeter water depth case. The same method was used to determine the inflow by matching the average velocity through the inlet and comparing to the PIV laboratory data.

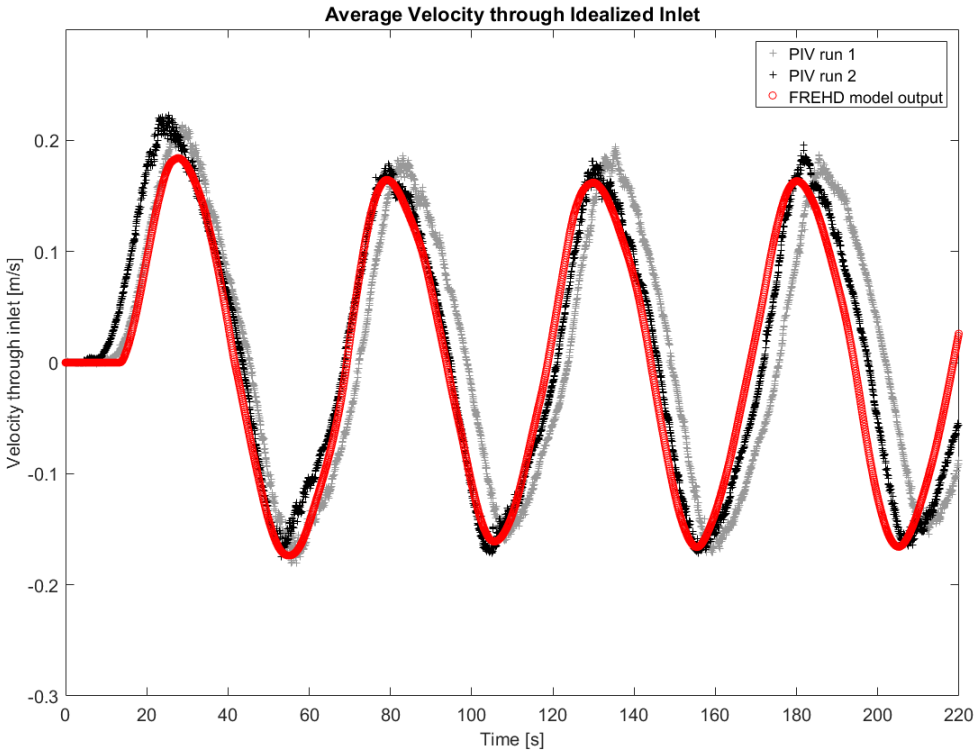

Figure 5.9: Average velocity through the inlet for the PIV laboratory data and the model run with an idealized inlet configuration and 3 cm water depth.

Two runs were done within the laboratory for the three centimeter water depth. The model matches the amplitude of both laboratory runs well. The first and second PIV runs have maximum values for tidal cycles 2 through 4 of approximately 0.18 $\frac{m}{s}$ and 0.17 $\frac{m}{s}$

respectively. The model predicts a maximum velocity through the inlet of 0.168 $\frac{m}{s}$. There is a slight phase difference between the two PIV laboratory cases. This demonstrates the level of repeatability of the laboratory experiments using the manual tidal reversal. The average phase difference between the two peaks for the PIV laboratory cases is 4.3 seconds. The model predicts a phase similar to the second PIV run. For the remainder of this section, the second PIV laboratory run will be used for comparison to the model results.

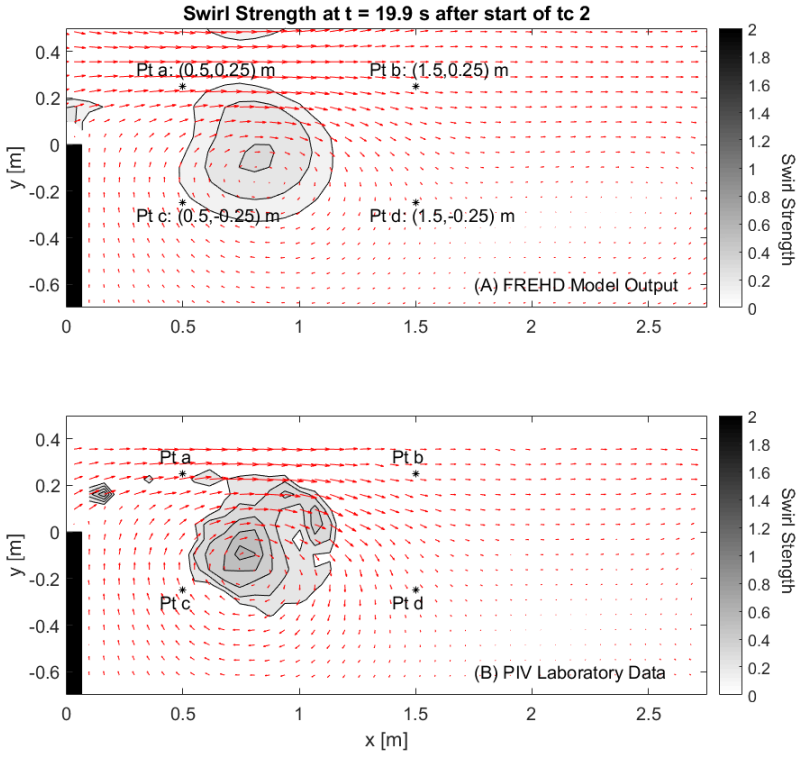

Figure 5.10: Swirl strength contour plot for (A) FREHD model run and (B) PIV laboratory data for idealized inlet configuration and 3 cm water depth

The vortex behavior for the 3 cm water depth case is similar to the 5 cm water depth case. The vortices spin up at the mouth of the inlet, detach, and propagate away from the inlet. Secondary vortices also form and eventually orbit around the primary vortex.

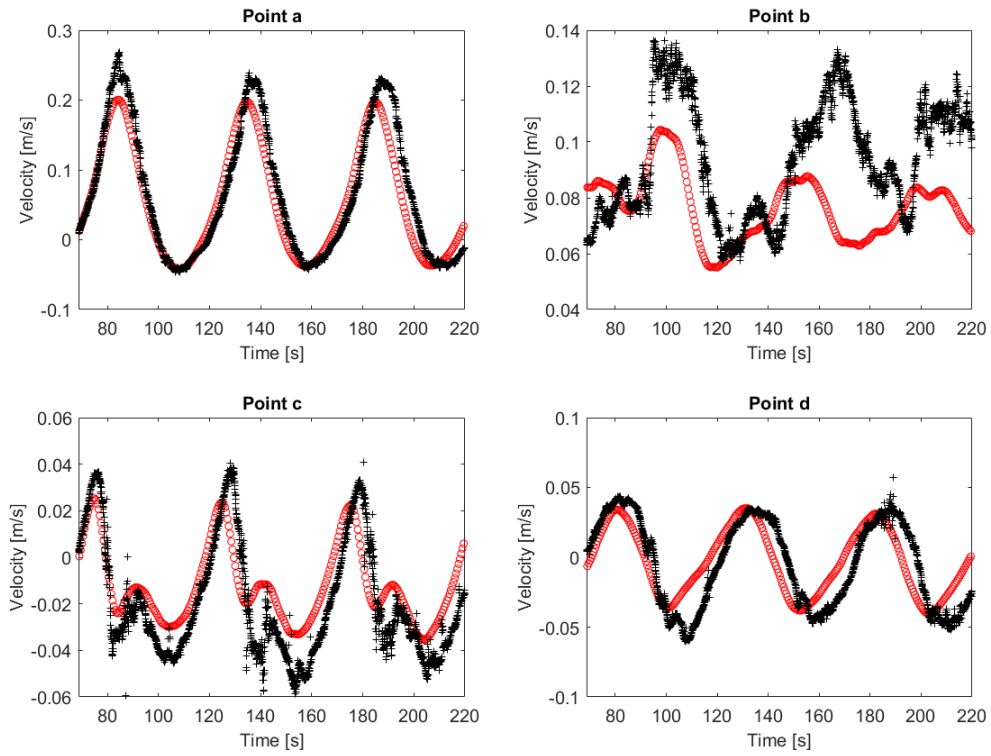

Figure 5.11: X-directed velocity at point a-d for idealized inlet configuration and 3 cm water depth

The locations of points a-d were adjusted from the 5 cm water depth case since the vortices do not propagate as far from the inlet as in the 5 cm water depth case. The points chosen are located at x distances of 0.5 and 1.5 m away from the inlet to better capture velocities affected by the vortices. The velocities in the x direction show similar trends to the 5 cm water depth case for points a and c. Point a shows a sharp peak and a rounded trough for both the PIV laboratory data and the FREHD model, as seen in the 5 cm water depth case. The model predicts the magnitude of the troughs relatively well but misses the peaks. At point c, the model predicts the double peaked trough that is also reflected in the PIV data which is also seen in the 5 cm water depth case. At point b, neither the magnitude

nor phase agree well in the model prediction. The shape of the x-directed velocity profile at point d is different than what was shown for the 5 cm water depth case but matches well between the PIV laboratory data and the FREHD model. In this case, the PIV laboratory data and model have a smooth shape with rounded peaks and troughs whereas the 5 cm case showed rounded peaks but sharp troughs [Figure 5.11].

The rms error for the x-directed velocities ranged from 0.0153 to 0.032 $\frac{m}{s}$. The characteristic velocity chosen for this flow is the maximum average velocity through the inlet. The characteristic velocity was used to normalize the rms errors to dimensionless values. The normalized rms error for the x-directed velocities ranged from 0.0909 to 0.1902. The maximum rms error occurred at point a and the minimum occurred at point c [Table 5.4].

Table 5.4: RMS Error for idealized inlet configuration with 3 cm water depth

Point	u component rms error [$\frac{m}{s}$]	u component normalized rms error	v component rms error [$\frac{m}{s}$]	v component normalized rms error
a	.0320	0.1902	0.0113	0.0674
b	0.0259	0.1543	0.0114	0.0680
c	0.0153	0.0909	0.0326	0.1941
d	0.0190	0.1131	0.0202	0.1204

The y-directed velocities show good phase agreement at all four points. The model generally misses the larger negative velocities at points c and d and the larger positive velocities at point a [Figure 5.12]. The rms error for the y-directed velocities ranges from 0.0113 to 0.0326 $\frac{m}{s}$. Once the velocities are normalized by the characteristic velocity, the rms errors range from 0.0674 to 0.1941. The maximum and minimum rms errors occur at point c and point a respectively [Table 5.4]. Similar to the 5 cm water depth case, the 3 cm water depth model tends to underestimate the velocities at various points throughout the

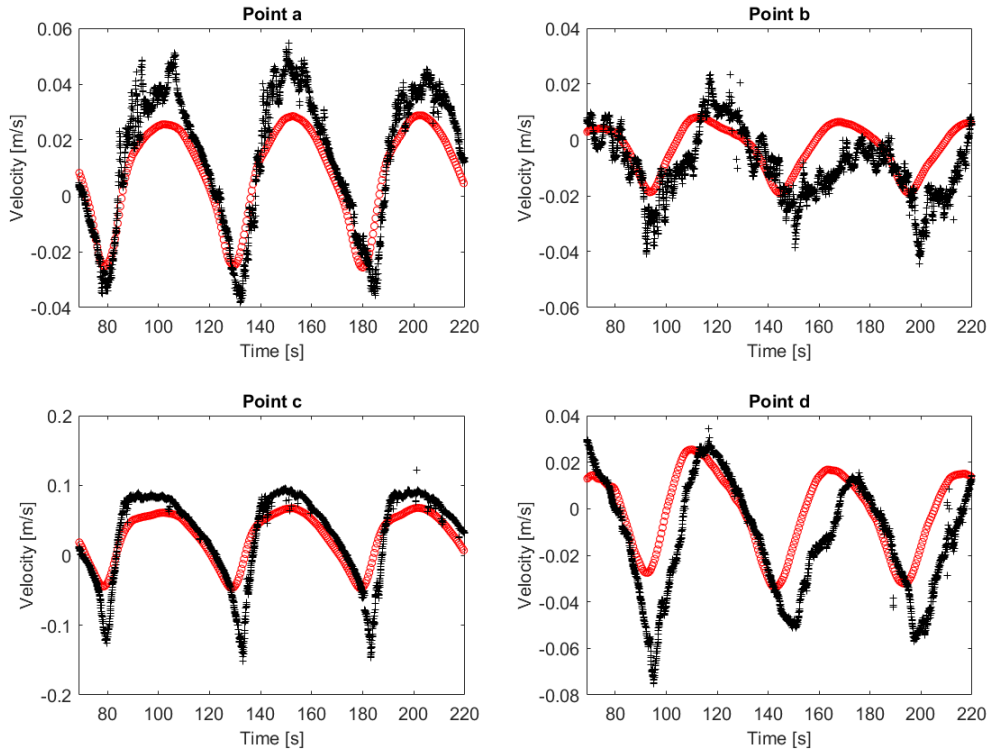

Figure 5.12: Y-directed velocity at point a-d for idealized inlet configuration and 3 cm water depth

domain but in general the phase agreement and shape of the profiles is consistent between the PIV laboratory data and the model with the exception of the x-directed velocity at point b.

The model predicts a maximum primary vortex diameter of approximately 0.64 meters. The maximum primary vortex diameter shown in the PIV laboratory data is approximately 0.61 m. Like the 5 cm case, the model again predicts slightly larger vortices than the PIV laboratory data shows. The model also reaches a peak vortex size approximately 3 seconds after the PIV laboratory data. The shape of the vortex diameter plot varies slightly between the model and laboratory data. Up until about 22 seconds from the start of each tidal

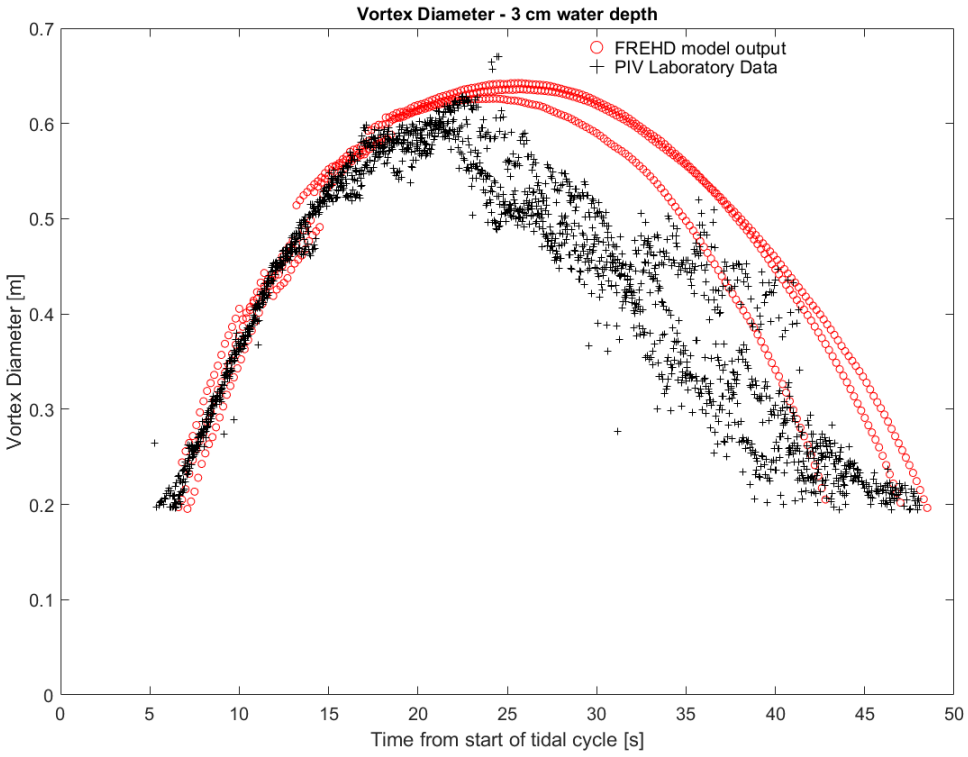

Figure 5.13: Primary vortex diameter over time for idealized inlet configuration with 3 cm water depth

cycle, the vortex diameter plot has the same shape for the model and laboratory data. After about 22 seconds, the PIV laboratory data begins to decrease at a constant rate whereas the model predicts the rate of decrease to increase over time.This is shown in the curved shape of the model prediction which remains after the vortex reaches its peak diameter [Figure 5.13]. The relative error of the model after about 25 s is 33% for vortex size which is similar to the error in the 5 cm depth case.

The vortex centroid location in space is similar for the model and PIV laboratory data. They show similar curves once the vortex detaches from the inlet, although the PIV laboratory data shows a stronger curve in the positive y direction than is predicted by the

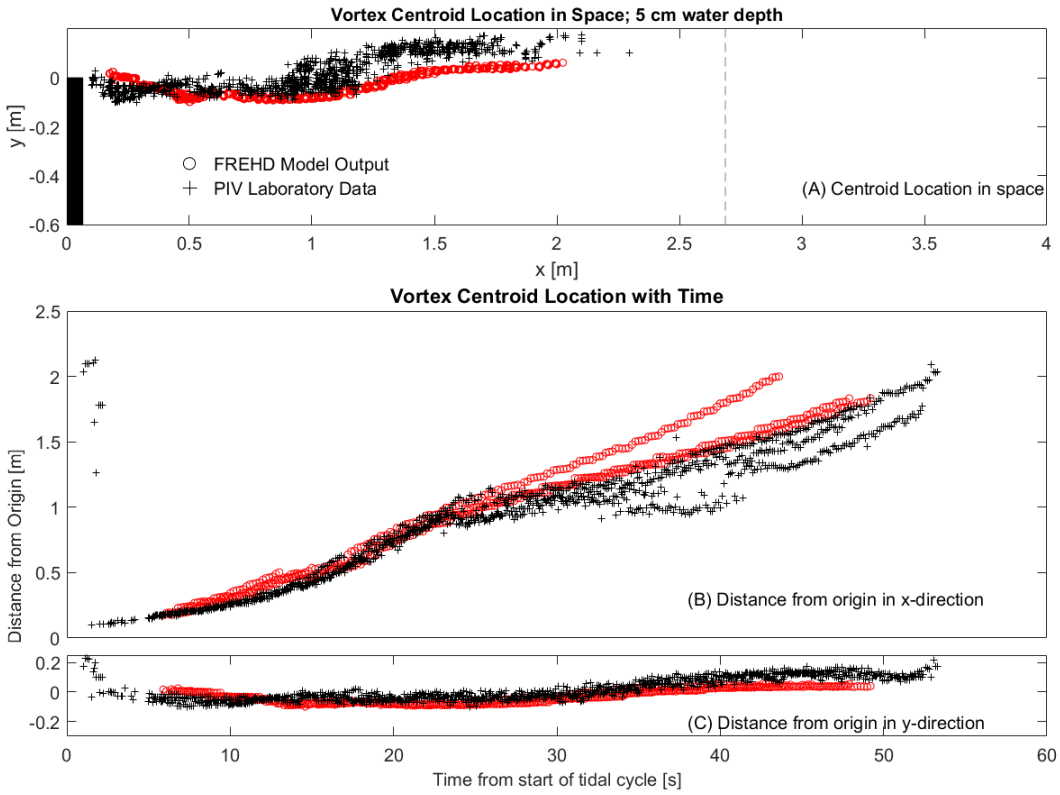

Figure 5.14: Location of the vortex centroid in (A) space and (B,C) time for idealized inlet configuration with 3 cm water depth

model. The model does a good job of predicting the maximum x location of the vortex which is at about 2 meters from the inlet for both the model and PIV laboratory data [Figure 5.14a]. This is where the vortex is arrested by the reverse tide. The vortex propagation time is also similar for the model and PIV laboratory data. The PIV laboratory data shows the vortices lasting for about 5 seconds longer than is predicted in the model. The slope of the plot of distance from the inlet in the x-direction over time for both the model and laboratory data are similar. The vortices move fast up until approximately 25 s of the tidal cycle and then propagate slower for the remainder of their lifetime [Figure 5.14b]. During the second half of the tidal cycles, the model does seem to show slightly faster vortex propagation

compared to the PIV laboratory data, but this is most likely because during that time the PIV laboratory data shows more motion in the y direction than the model predicts.

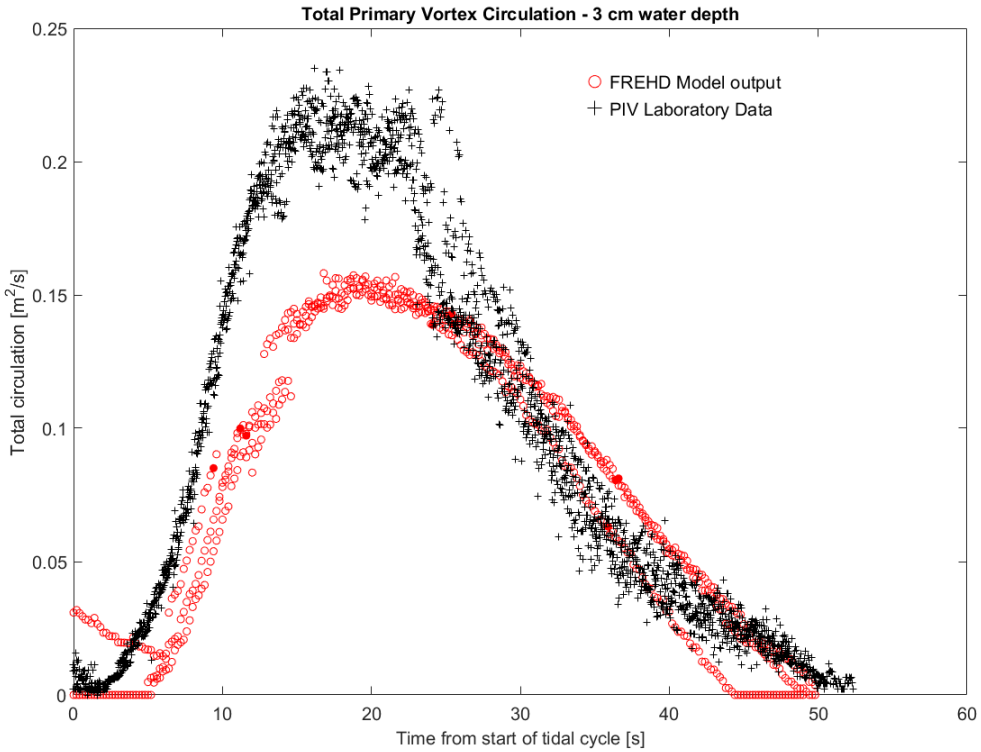

Figure 5.15: Total circulation within the primary vortex for the idealized inlet configuration with 3 cm water depth

The total circulation within the primary vortex for the three centimeter water depth has a similar trend to the five centimeter water depth case. About halfway through the tidal cycle, the model predicts the total circulation within the primary vortex well but from approximately 10 to 25 seconds the model is unable to capture all of the circulation that is shown in the PIV laboratory data. The maximum total circulation within the primary vortex for the laboratory data is approximately 0.23 $\frac{m^2}{s}$; whereas, the model only reaches a maximum value of 0.15 $\frac{m^2}{s}$. This difference is believed to be caused by the inability of

the FREHD model to resolve the secondary vortices or the boundary layer effects at the inlet. The overall shape of the total circulation within the primary vortex is the same for the model and laboratory data. The model also reaches a peak value at approximately the same time as the laboratory data. This peak occurs about 20 seconds after the start of each tidal cycle.

The overall agreement of the circulation for the 3 cm water depth is slightly better than for the 5 cm case. However, circulation is a combination of vorticity and the area. For the shallower case, the model overpredicts the vortex size by a greater amount, which allows the total circulation to have lower error.

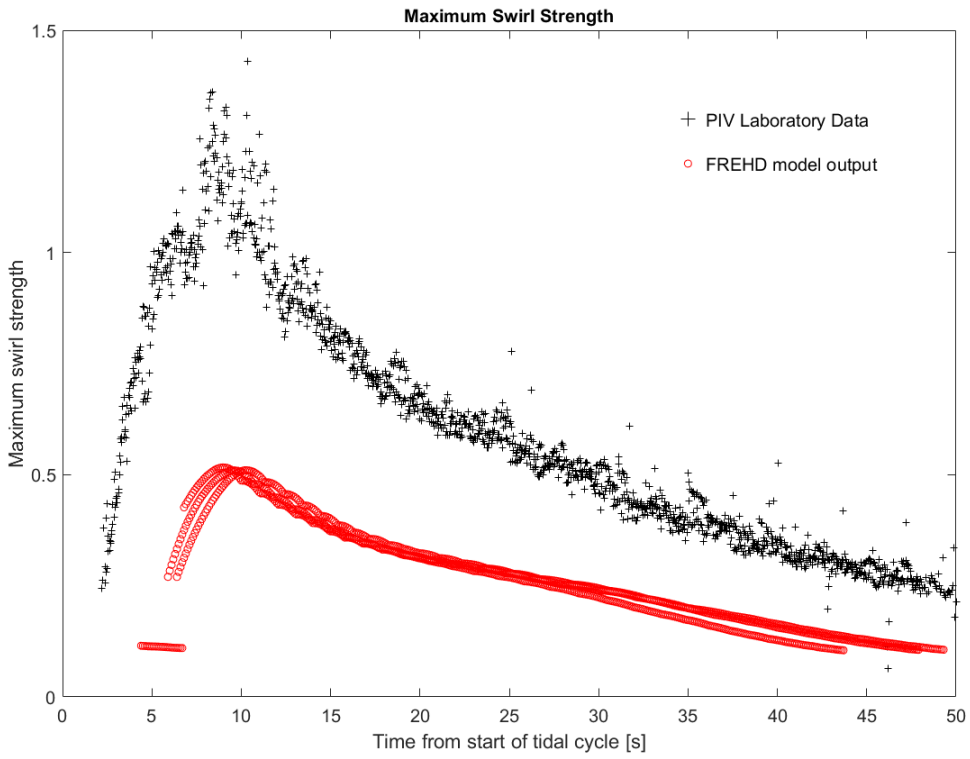

Figure 5.16: Maximum swirl strength within the primary vortex for a 3 cm water depth and idealized inlet configuration

The FREHD model under predicts the maximum swirl strength within the primary vortex. The swirl strength reaches a maximum of 1.4 $\frac{1}{s}$ in the PIV laboratory data but the model predicts a maximum value of 0.55 $\frac{1}{s}$. The model and PIV laboratory data both show a peak approximately 10 seconds after the start of each tidal cycle and have the same overall shape.

5.1.3 Nine Centimeter Water Depth

The final case of model validation for the idealized inlet configuration was done with a nine centimeter water depth.

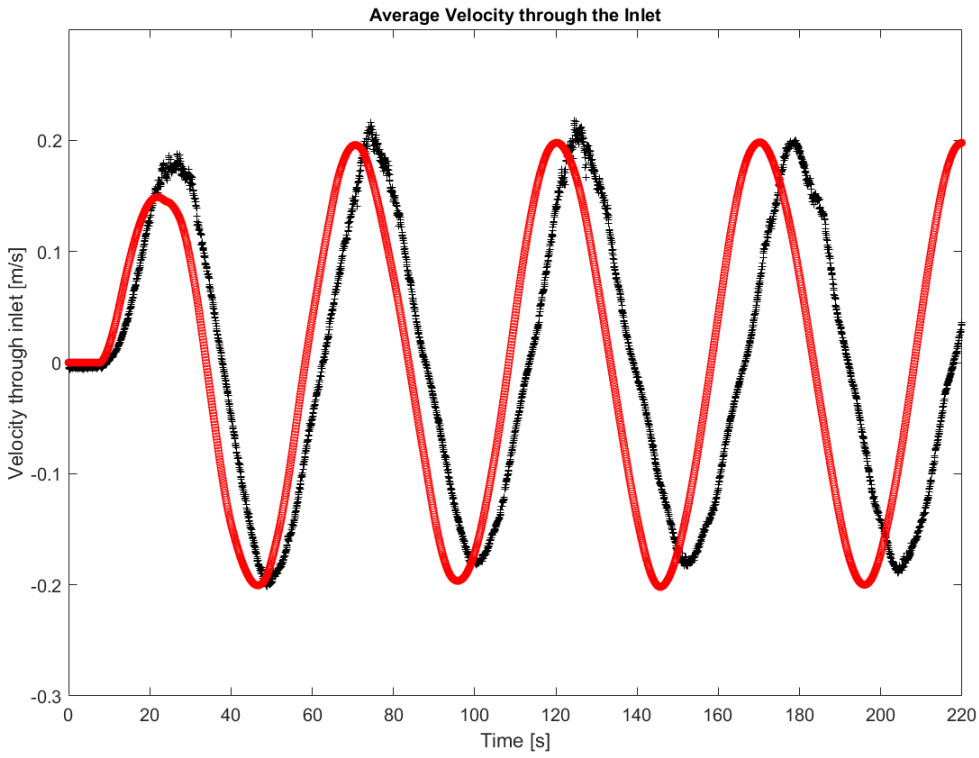

Figure 5.17: Average velocity through the inlet for idealized inlet configuration with 9 cm water depth

The inflow was adjusted until the magnitude of the average velocity through the inlet adequately matched for the FREHD model and laboratory data. The maximum average velocity through the inlet for the PIV laboratory data was 0.217 $\frac{m}{s}$ and the mean peak velocity for tidal cycles 2 through 4 is 0.211 $\frac{m}{s}$. The model predicted a maximum velocity through the inlet of 0.20 $\frac{m}{s}$ with a mean peak velocity of 0.197 $\frac{m}{s}$. The relative error at the peaks, excluding the first tidal cycle, was at a maximum during the second tidal cycle with a relative error of 9.6%. The mean relative error in the magnitude of the peaks for tidal cycles 2 through 4 is 6.4%. There is a growing phase lag with time for the velocity through the inlet. At the beginning of the second tidal cycle, the phase lag is 4.3 seconds or 8.5% of the tidal period. The phase lag grows to a maximum of 9.67 seconds or 19.3% of the tidal period by the end of the fourth tidal cycle. No attempt was made to adjust the tidal period within the model since this was a known parameter within the laboratory experiments. However, the model predicted a shorter period within the inlet than the PIV laboratory data showed [Figure 5.17], which may indicate that the PIV experiments had a slightly longer period than reported due to errors in manually reversing the flow.

The phase lag does not play an important role in comparing the model to the measured data. The starting jet vortices for this case form quickly and proagate out of the PIV field of view before tidal reversal. Hence, as long as the model matches the peak velocity and has a similar period, small phase errors can be neglected in comparing vortex properties.

The nine centimeter water depth shows similar results to the other two water depths. The magnitude of the swirl strength is generally greater in the PIV laboratory data than

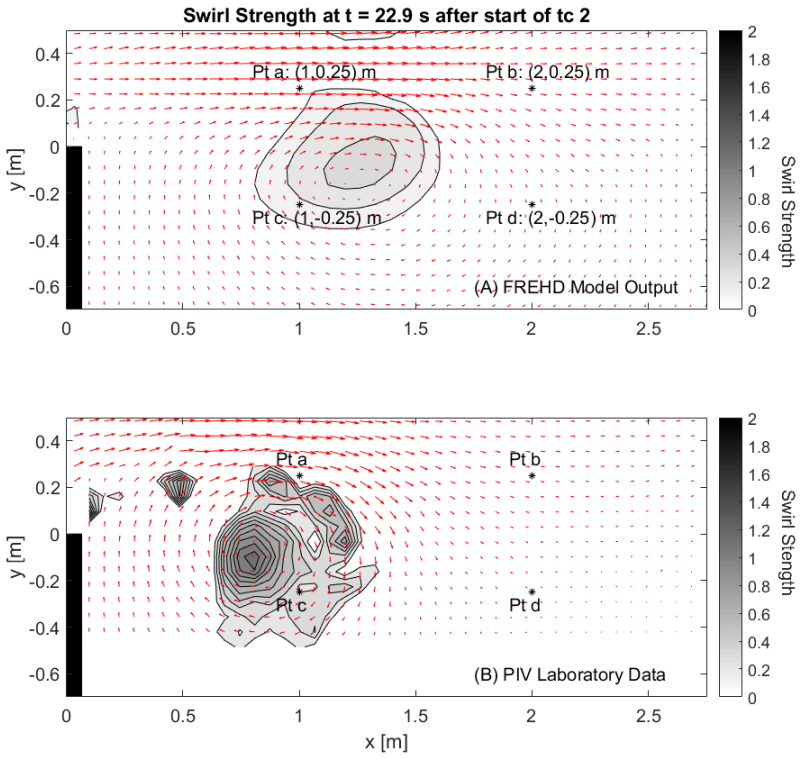

Figure 5.18: Average velocity through the inlet for idealized inlet configuration with 9 cm water depth

the model predicts. There are also secondary vortices which can be seen in the laboratory data that are not present in the model. For the other two water depths, the data showed the location of maximum swirl strength near the center of the vortex for both the model and PIV laboratory data. In this case, the model still shows the location of maximum swirl strength near the center of the vortex but in the PIV laboratory data the vortex is much less symmetric [Figure 5.18]. The location of maximum swirl strength occurs closer to the inlet side of the vortex and then there are secondary vortices on the far side of the inlet which look like they have begun to join the primary vortex. Although only one instant is shown in the figure, the asymmetric nature of the vortex must be considered when analyzing the

velocities surrounding the vortex.

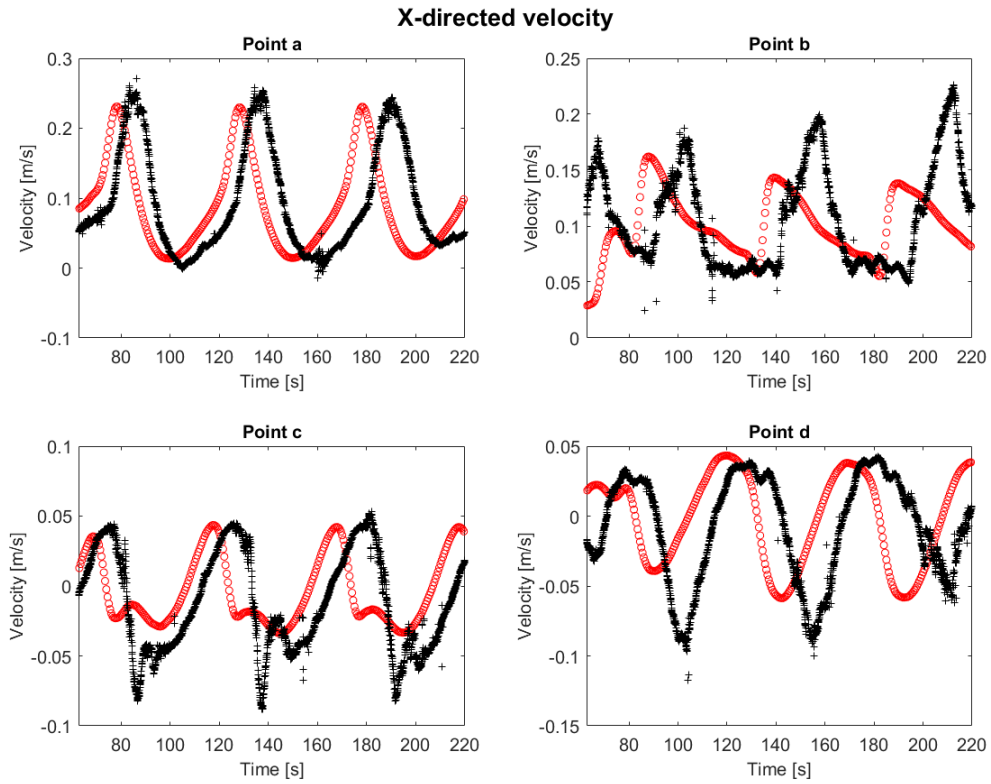

Figure 5.19: X-directed velocity at point a-d for the idealized inlet configuration with 9 cm water depth

The phase lag seen in Figure 5.17 is also apparent at each of the four points a-d used to compare velocities throughout the domain. At point a, the velocity in the x direction shows the same shape as the PIV laboratory data. The magnitude of the peaks are slightly greater for the laboratory data than the model predicts, though the disparity is less than in the shallower cases. The phase lag also grows with time. The results at point c are similar to point a. The overall shape of the velocity time series agrees with the model results but the model misses sharp negative spikes present in the PIV laboratory data. At point b there are many discrepancies between the laboratory and model results. The peak velocity at

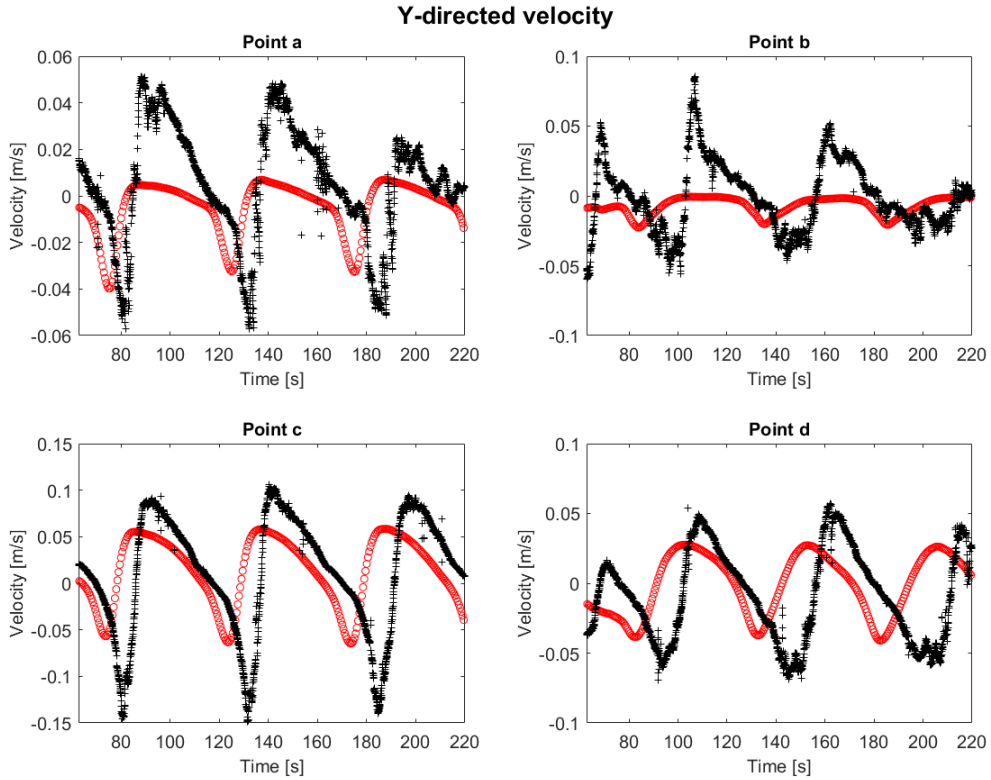

Figure 5.20: Y-directed velocity at point a-d for the idealized inlet configuration with 9 cm water depth

point b in the model tends to decrease in magnitude with each tidal cycle; whereas, the PIV laboratory data shows an increase in peak velocity reaching a maximum during the fourth and final tidal cycle. The shape of the PIV laboratory data shows a gradual increase to the peak velocity and then a sharp drop followed by the leveling off of the velocity for about 20 seconds before reaching the next peak. The model predicts a sharp increase to the peak velocity and then a gradual drop in velocity lasting until the next peak. At point d, the shape of the model and laboratory data agree well at the peaks but the model predicts a rounded trough and the PIV laboratory data shows a sharp trough [Figure 5.19].

The velocity in the y direction is similar to the x-directed velocities at points a through

d. The phase lag is also present as seen in Figures 5.17 and 5.19. At points a and c the model does not predict the high positive velocities seen in the PIV laboratory data [Figure 5.20].

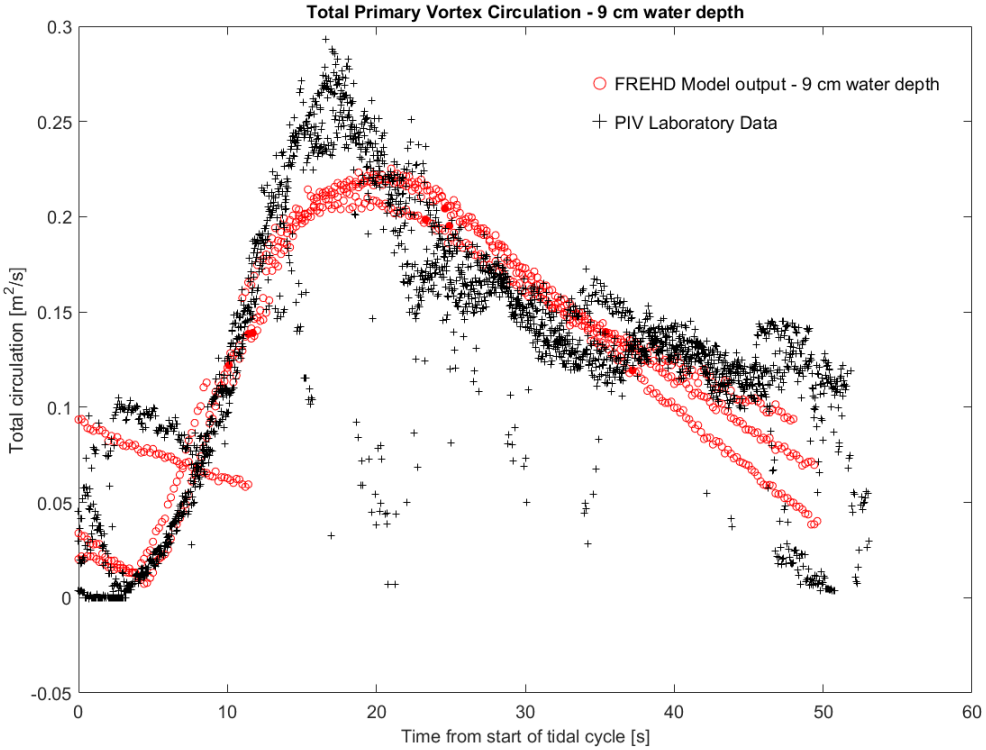

Figure 5.21: Total circulation within the primary vortex for the idealized inlet configuration with 9 cm water depth

The total circulation within the primary vortex agrees well with the PIV laboratory data except for the peak between 14 and 20 s, which is not predicted by the model [Figure 5.21]. It is important to note that the circulation is calculated by integrating over the area of the primary vortex according to Equation 3.3. Figure 5.22 shows that the difference in vortex diameter for the model and PIV laboratory data reaches a maximum of approximately 0.25 meters when the vortex in the model reaches a maximum diameter of 0.7 meters and

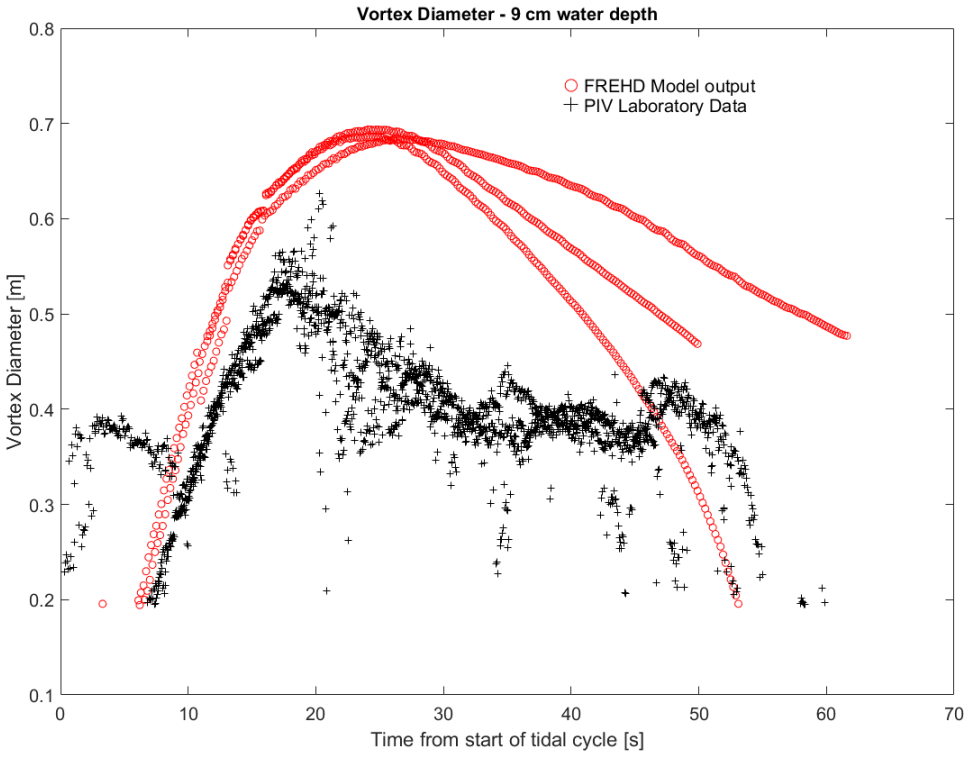

Figure 5.22: Primary vortex diameter for the idealized inlet configuration with 9 cm water depth

the PIV laboratory vortex diameter is only 0.45 meters. When calculating the total circulation for the PIV laboratory data, the integration would be over an area of approximately 0.16 m^2 whereas the model would be integrating over an area of 0.38 m^2. The integration area is almost doubled at this point. Even though the circulation appears to agree well, the difference in size must be considered in making an overall assessment. The model predicts a good circulation, but spreads the weaker vorticity over a larger area.

The centroid location for the nine centimeter water depth is similar for the model and PIV laboratory data. Figure 5.23b shows that the vortices are moving at roughly the same speed since the slope of the lines are similar for the model and PIV laboratory data. The

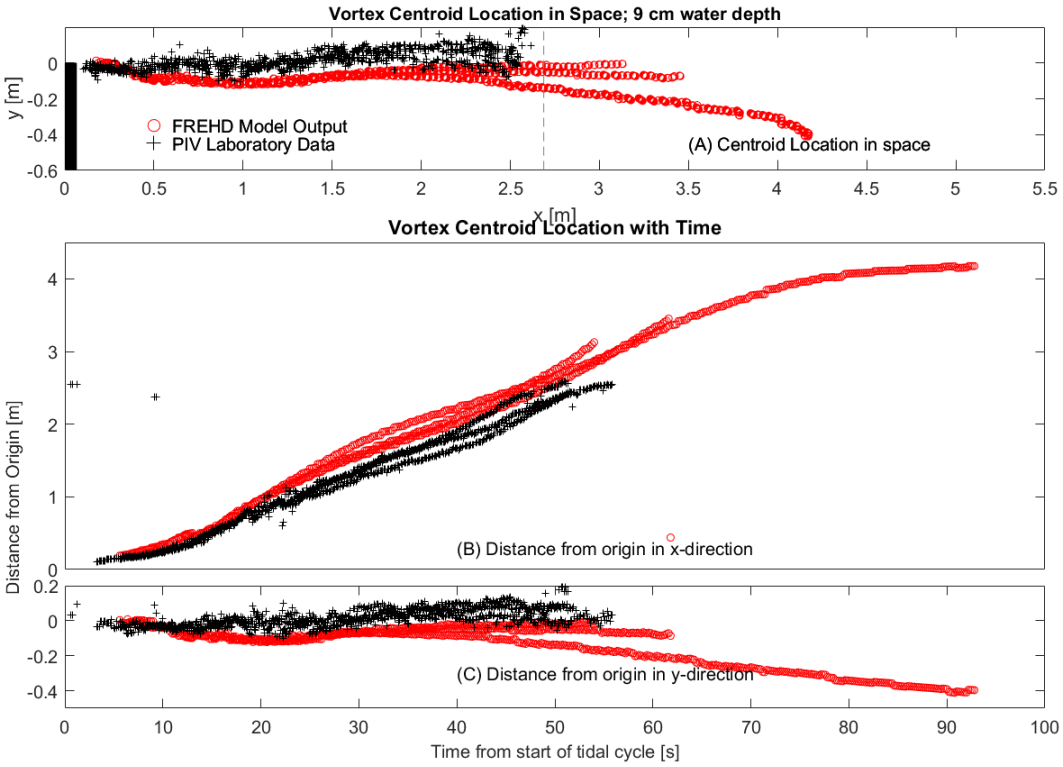

Figure 5.23: Vortex centroid location in (A) space and (B,C) time for the idealized inlet configuration with 9 cm water depth

PIV laboratory data is consistently located closer to the inlet than the model predicts. This can be seen in Figure 5.18 as well. The vortex in the PIV laboratory data also tends to have a straighter trajectory than the model predicts [Figure 5.23c]. The error in the centroid location in space and time is similar to the shallower cases.

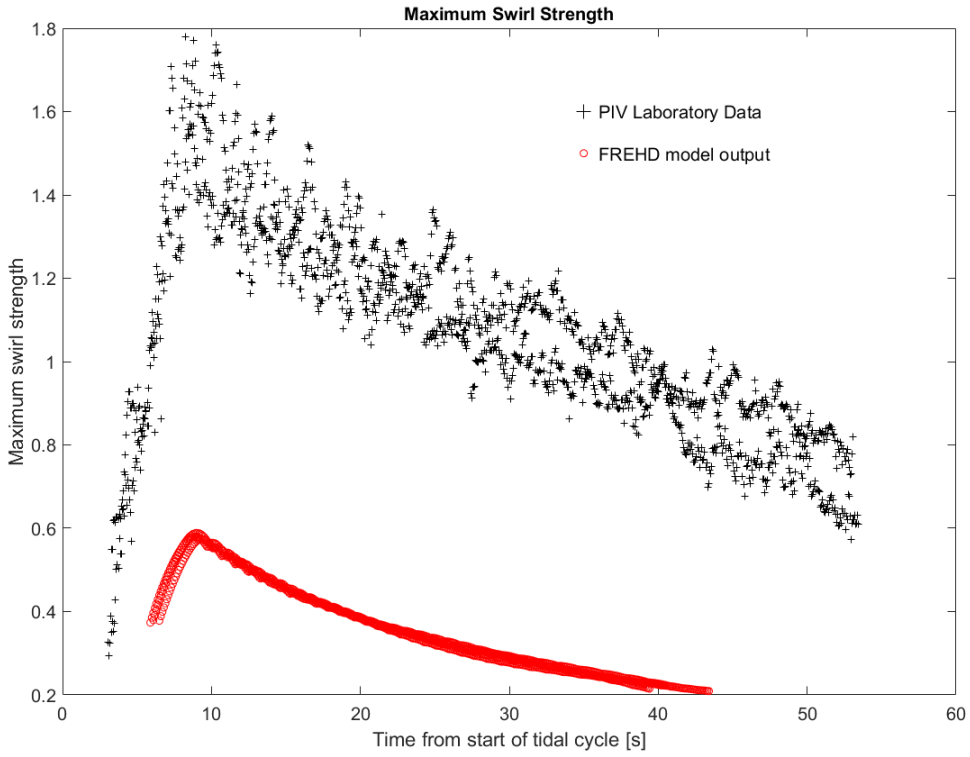

Figure 5.24: Maximum swirl strength within the primary vortex for 9 cm water depth and idealized inlet configuration

Similar to the other two water depths, the FREHD model under predicts the maximum swirl strength within the primary vortex. The maximum swirl strength from the laboratory data reaches approximately 1.8 s^{-1}, but the model predicts a maximum value of 0.6 s^{-1}. The shape of the two profiles are similar for the model and laboratory data. Once the PIV laboratory data reaches a maximum, the maximum value decreases linearly with time until the vortex fully dissipates. The model shows a similar trend but the decrease from the maximum shows a slight curve with time unlike the PIV laboratory data.

The nine centimeter water depth shows the worst agreement between the model and

PIV laboratory data of the three idealized inlet configuration cases. Although a water depth of nine centimeters is still a shallow flow, the vortex is most likely more influenced by three-dimensional effects than the shallower cases. We hypothesize that the non-hydrostatic pressure terms will have increasing importance as the water depth increases. At higher water depths, there is more room for free surface motion. Free surface gradients may contribute to the coherent nature of the vortex and could contribute to the differences in vortex size between the model and laboratory data.

5.2 Other Inlet Configurations

The following two configurations have channel lengths of 1.35 in the wide barrier island and 1.11 m in the jettied case, respectively. Since these configurations have channel lengths on the order of the channel width, they require an understanding of the lateral boundary layer in the channel. With a large boundary layer, there is an additional vortex that forms at the start of ebb tide called the expelled boundary layer vortex [5]. The expelled boundary layer vortex was not seen during every tidal cycle throughout the laboratory experiments, but the expelled vorticity from the boundary layer always affected the primary starting jet vortex. When the expelled boundary layer vortex did form, the laboratory experiments showed two possible interactions between the expelled boundary layer vortex and the primary starting jet vortex [5].

The behavior depended on the size of the expelled boundary layer vortex. Mode 1 occurs when the expelled boundary layer vortex is small compared to the starting jet vortex.

In this case, the expelled boundary layer vortex forms a dipole with the primary starting jet vortex, deflecting the starting jet vortex at a 35 degree angle away from the inlet. The expelled boundary layer vortex then dissipates shortly after the primary vortex moves away from the inlet. The second possible behavior, Mode 2, occurs when the expelled boundary layer is similar in size to the primary starting jet vortex. In this case, the vortices form quickly and propagate together at a 20 degree angle [5].

5.2.1 Large Barrier Island

The next configuration run within the FREHD model was the large barrier island case. As for the previous cases, the inflow was adjusted until the average velocity through the inlet matched for the PIV laboratory data and the FREHD model.

The FREHD model was able to predict the average velocity through the inlet well [Figure 5.25]. The amplitude of the curve matched within 0.02 $\frac{m}{s}$, aside from the second tidal cycle which showed some increased velocities when the PIV laboratory data first reached a maximum. There is a growing phase lag with time between the PIV laboratory data and the model output. The start of the second tidal cycle in the PIV data occurs 2.91 seconds before the model prediction. This phase lag grows to 5.5 seconds by the start of the fourth tidal cycle. The mean tidal period for the PIV laboratory data is 48.8 seconds and the mean tidal period for the FREHD model is 50.1 seconds so the tidal period agrees within about 1 second for tidal cycles two through four [Figure 5.25].

The laboratory experiments for the large barrier island case showed the formation of an expelled boundary layer vortex for the second and third tidal cycles. Mode 1 behavior

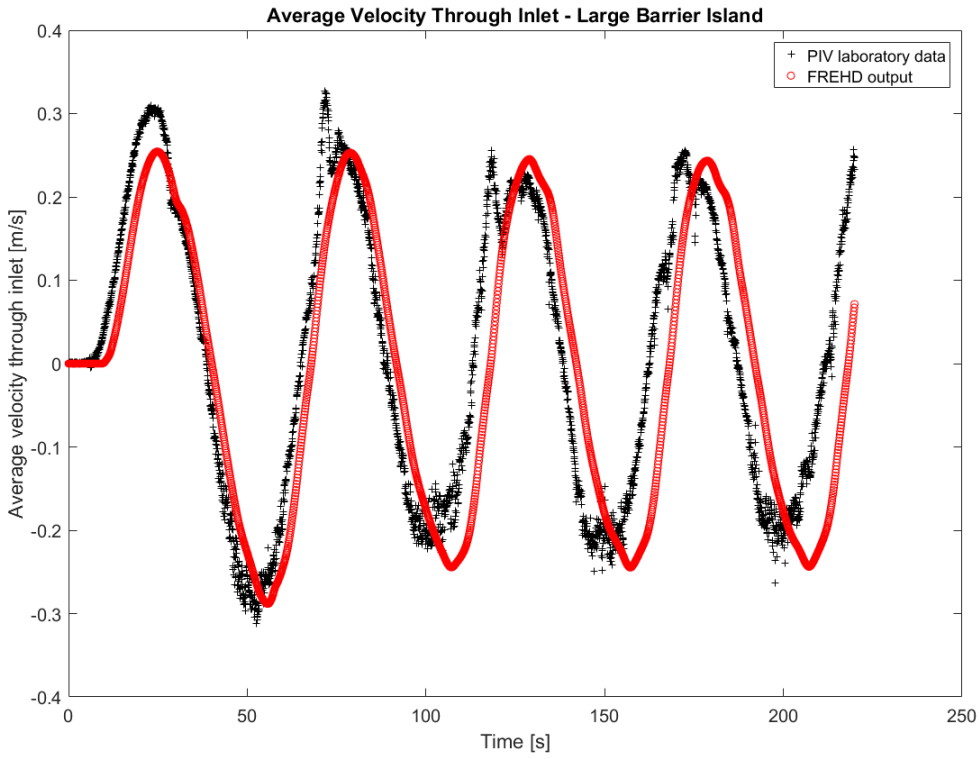

Figure 5.25: Average velocity through the inlet for the large barrier island configuration

was observed for the second tidal cycle and Mode 2 behavior was observed for the third tidal cycle.

In the PIV laboratory data, the expelled boundary layer can be seen clearly after a fourth of the second tidal cycle. The dipole between the vortices cause propagation at a 35 degree angle as described above [Figure 5.26A]. The FREHD model is unable to capture this behavior. In Figure 5.26B, a small expelled boundary layer vortex forms in the model, but the vorticity within the vortex is not strong enough to form a dipole with the primary starting jet vortex. Without the dipole formation, the trajectory of the starting jet vortex is unchanged from the idealized case. We expect that the under-prediction in the model of

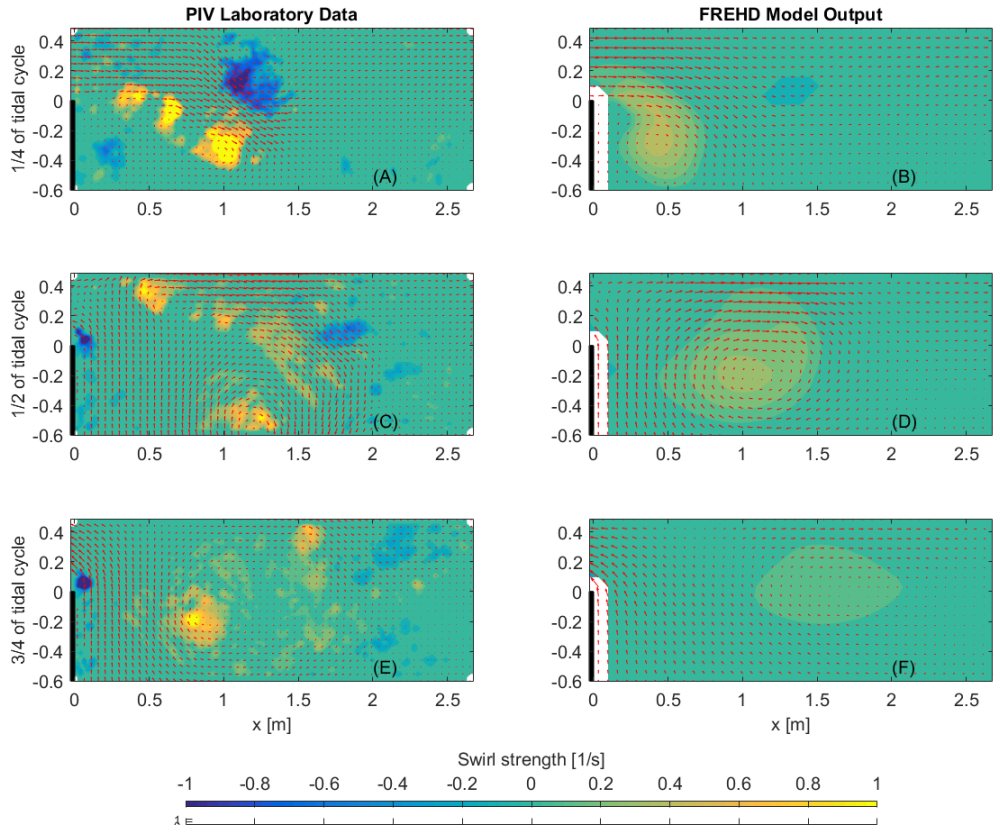

Figure 5.26: Swirl strength for PIV laboratory data and FREHD model at (A,B) 1/4 of the second tidal cycle, (C,D) 1/2 of the second tidal cycle, and (E,F) 3/4 of the second tidal cycle multiplied by the sign of the vorticity for the large barrier island configuration

the vorticity and swirl strength, two parameters describing the strength of the vortices, is the main reason the expelled boundary layer vortex does not pair with the primary vortex.

During the third tidal cycle of the laboratory data, the expelled boundary layer vortex showed Mode 2 behavior. One quarter through the third tidal cycle the expelled boundary layer vortex and primary starting jet vortex have formed a dipole [Figure 5.27A]. By halfway through the third tidal cycle, the vortices propagated to the bottom right corner of the PIV field of view [Figure 5.27C] and by three quarters of the tidal cycle the vortices are no longer visible [Figure 5.27E]. The FREHD model did not show any expelled

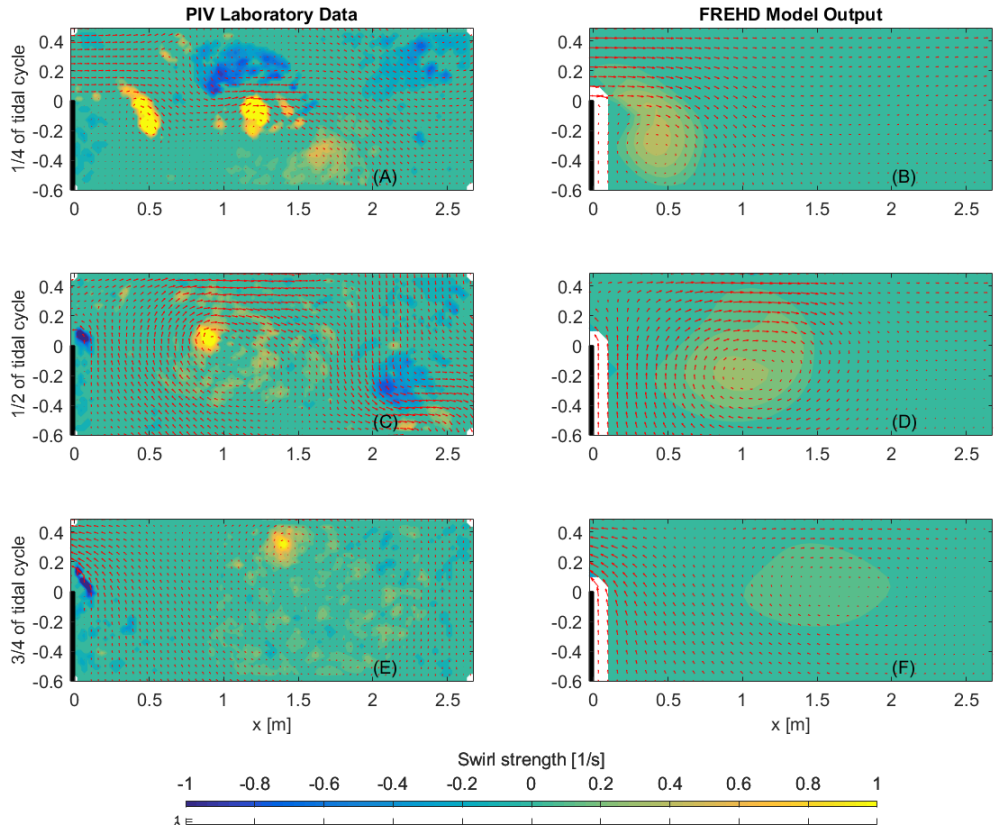

Figure 5.27: Swirl strength for PIV laboratory data and FREHD model at (A,B) 1/4 of the third tidal cycle, (C,D) 1/2 of the third tidal cycle, and (E,F) 3/4 of the third tidal cycle multiplied by the sign of the vorticity for the large barrier island configuration

boundary layer formation during the third tidal cycle. The vortex in the FREHD model behaves similarly to the primary starting jet vortex behavior in the idealized inlet configuration case [Figure 5.27B;D;F]. Hence, the model does not capture the boundary layer vortices correctly.

5.2.2 Long Jetty

The final configuration run within the FREHD model is the long jetty configuration. The channel length in the configuration is also on the order of the inlet width so the boundary layer plays an increasing role.

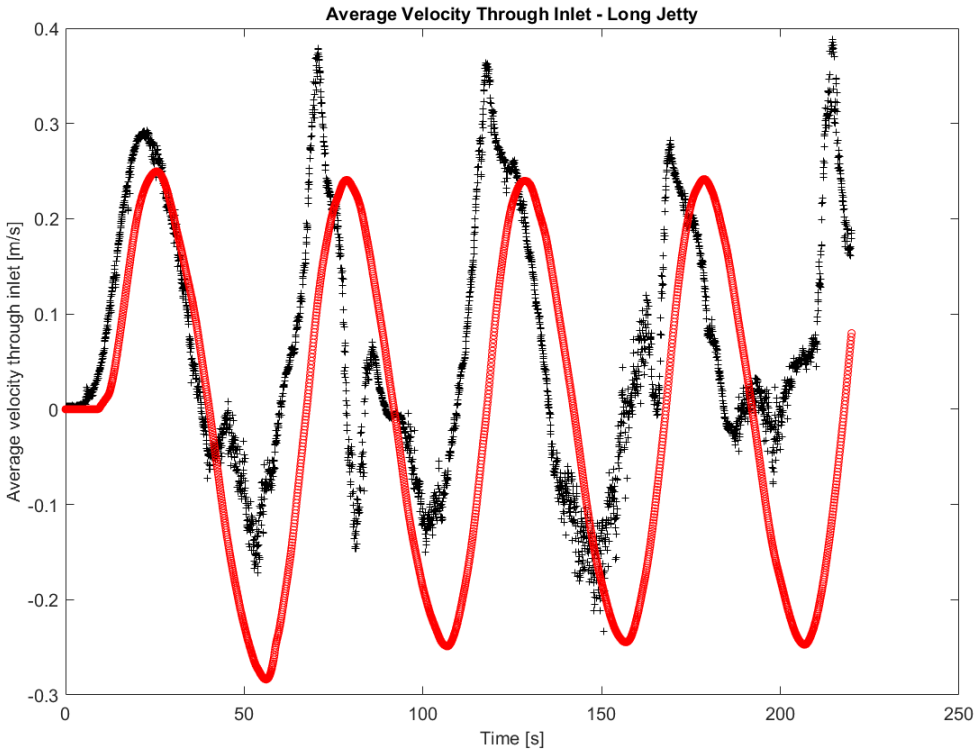

Figure 5.28: Average velocity through the inlet for the long jetty configuration

The inflow was adjusted as best as possible within the FREHD model to attempt to match the PIV laboratory data. There are still some discrepancies between the model and laboratory results. The PIV laboratory data shows an asymmetrical amplitude. The velocities through the inlet for the laboratory data reach a maximum of 0.39 $\frac{m}{s}$ during ebb tide but only reach a maximum of 0.23 $\frac{m}{s}$ on the reverse tide. The FREHD model is unable to replicate this asymmetry likely due to errors in the vortex behavior. The FREHD model predicts a maximum velocity of 0.25 $\frac{m}{s}$ during ebb tide, but on reverse tide the model predicts a maximum value of 0.28 $\frac{m}{s}$. Since the asymmetry is not mirrored, adjusting the inflow in either direction does not correct the differences between the model and laboratory

results.

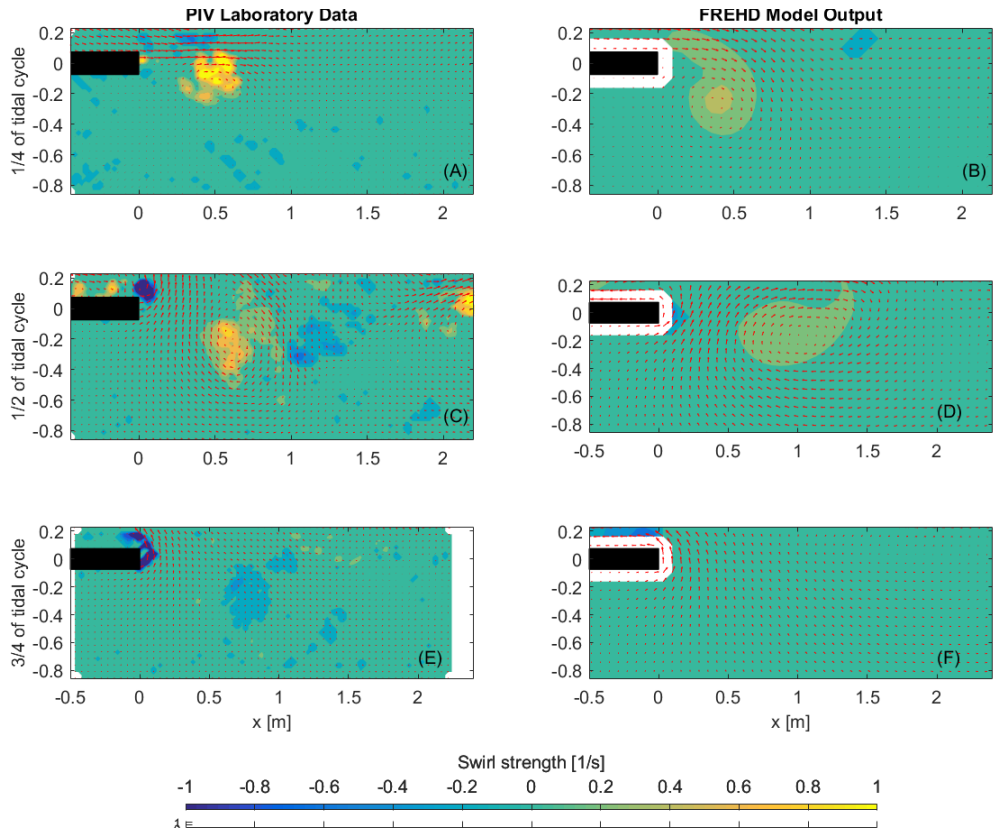

Figure 5.29: Swirl strength for PIV laboratory data and FREHD model at (A,B) 1/4 of the tidal cycle, (C,D) 1/2 of the tidal cycle, and (E,F) 3/4 of the tidal cycle multiplied by the sign of the vorticity

For the long jetty configuration, the PIV laboratory data shows interaction between the primary starting jet vortex and the expelled boundary layer vortex after one quarter of the tidal cycle. The vortices form at approximately the same time and begin to propagate away from the inlet together [Figure 5.29A]. The FREHD model predicts a small expelled boundary layer vortex but it forms before the starting jet vortex and propagates away from the inlet with no interaction with the starting jet vortex [Figure 5.29B]. The existence of the expelled boundary layer changes the trajectory of the starting jet vortex within the

PIV laboratory data and causes propagation at an angle [Figure 5.29C]. Since the expelled boundary layer vortex has already dissipated by halfway through the tidal cycle, the starting jet vortex in the FREHD model propagates away in a straight path similar to the idealized inlet configuration.

The results of the idealized inlet configuration showed that the FREHD model does not produce the high vorticity and swirl strength values seen in the PIV laboratory data. Without these high vorticities in the other configurations, the expelled lateral boundary layer is less energetic and is unable to produce a strong enough vortex to cause interaction with the primary starting jet vortex. As a result, the model performance becomes weaker as vortex interactions become more important.

5.3 Possible Model Improvements

The FREHD model does have other options that were considered after the base case was chosen for this thesis. These possible improvements will be described here, which include adding the non-hydrostatic pressure terms, upgrading the turbulence closure model, and implementing a higher order advection scheme. Some of these improvements have been successfully run in the FREHD model; whereas, other improvements cannot be run successfully in FREHD without modifications to the current code.

5.3.1 Non-Hydrostatic Pressure Terms

The non-hydrostatic pressure terms were added to the FREHD model and run with all of the same parameters descibed in Section 2.2.

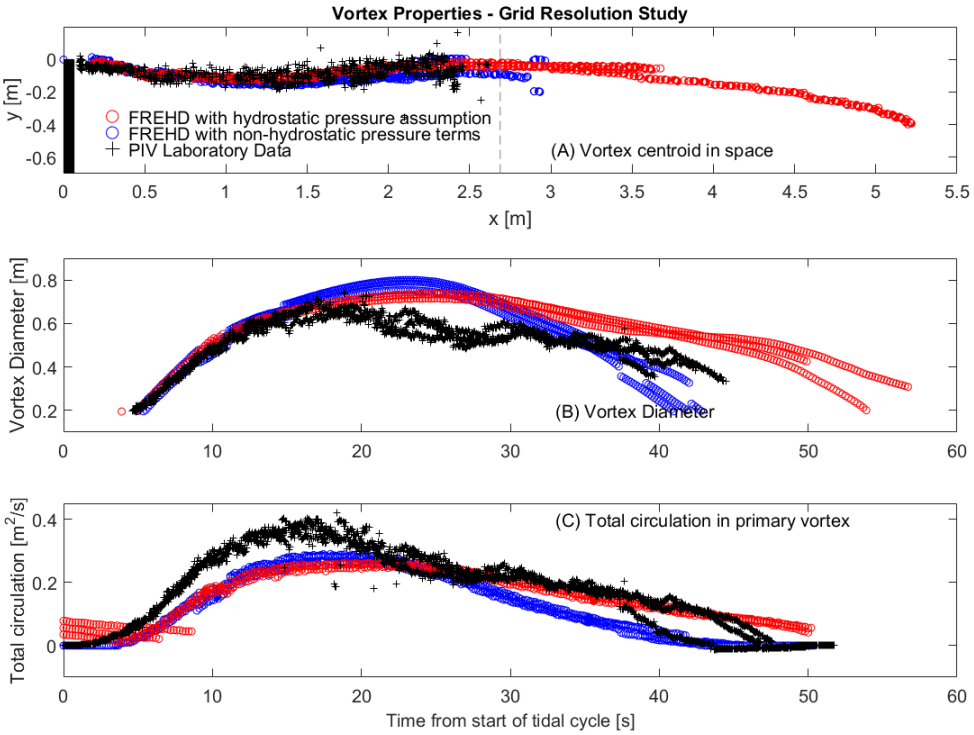

Figure 5.30: (A) Vortex centroid location in space, (B) Vortex diameter, and (C) total circulation in primary vortex for PIV laboratory data, FREHD model with hydrostatic pressure assumption, and FREHD model with non-hydorstatic pressure terms turned on.

The vortex diameter and circulation are similar with a hydrostatic and non-hydorstatic pressure assumption. The trajectory of the centroid is similar up until the end of the PIV field of view. After the vortex travels outside of the PIV field of view, the vortex with a hydrostatic pressure assumption travels about 2 m further than in the non-hydorstatic case. Since there is no laboratory data past the end of the PIV field of view, there is no way to validate which prediction is correct.

In order for the non-hydrostatic pressure terms to be important there needs to be some non-hydrostatic process occurring within the flow. There are no large free surface

variations within the flow, so the free surface gradients are not likely to be the driving force anywhere throughout the domain. We have shown that the secondary vortices are important especially to the total circulation within the primary vortex but we have no reason to believe that the secondary vortex formation is a non-hydrostatic process. The vortices most likely form due to two-dimensional (depth-average) boundary layer separation at the sharp corner of the inlet. Since there are no obvious non-hydrostatic processes occurring within the flow, a hydrostatic pressure assumption is likely sufficient.

5.3.2 Turbulence Closure

The current turbulence closure model used for all model runs in this thesis was a one-equation turbulence model that solves an additional transport equation for the turbulent kinetic energy. The FREHD model also has a k-ε turbulence model included. The k-ε turbulence model has not been thoroghly tested so it is still possible that there are problems with the code. We believe that the k-ε turbulence model will not improve the results of the FREHD model. The majority of turbulence closure models provide closure for the vertical viscosity, however, the horizontal viscosity is generally calculated using a constant horizontal viscosity coefficient. Since the flow described here does not have significant vertical effects, the variance in the horizontal viscosity over the doamin is more imprtant than the vertical variance. We hypothesize that improving the turbulence closure by implementing a two-equation turbulence model such as k-ε would not significantly improve the model results.

5.3.3 Higher Order Advection Schemes

All model runs up until this point used a first order upwind advection scheme. This scheme has more numerical dissipation than higher order advection schemes. FREHD also has the ability to use a second-order centered scheme or a third order upwind scheme. In this section the results from a model run using a third order upwind advection scheme for a five centimeter water depth and idealized inlet configuration are compared to the results shown in Section 5.1.1. All other inputs to the model remain the same including the previously calibrated inflow value.

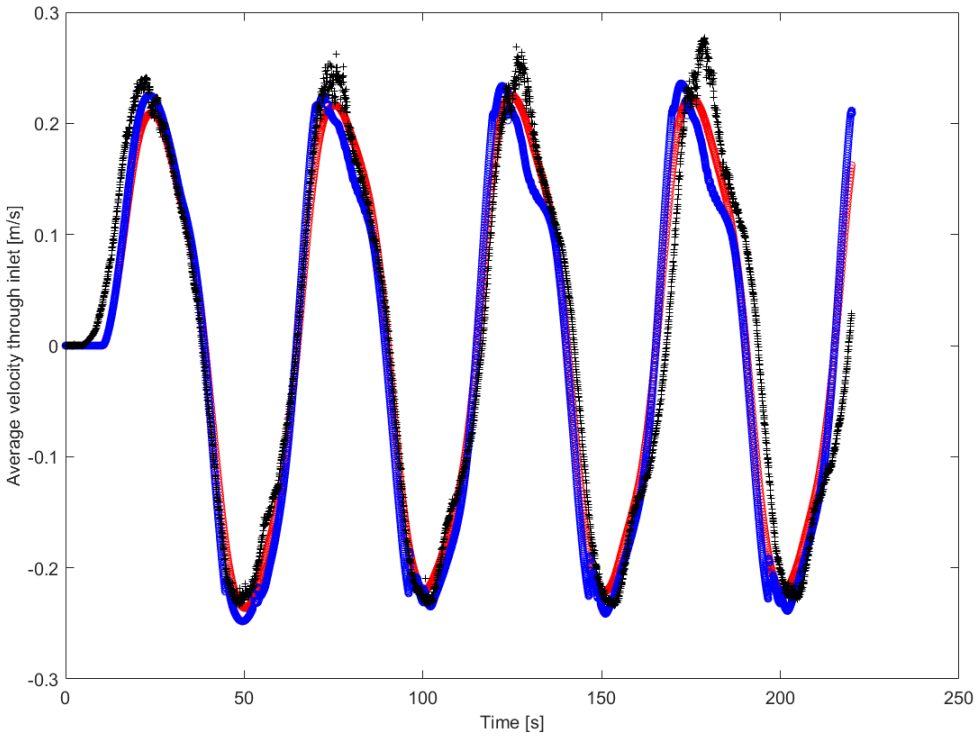

Figure 5.31: Average velocity through the inlet versus time.

Flow velocity through the inlet is similar for the third order and first order advection

schemes. The average velocity through the inlet for the laboratory PIV data reaches a maximum of 0.276 $\frac{m}{s}$ during the fourth tidal cycle. The model predicts a maximum value of 0.236 $\frac{m}{s}$. For tidal cycles 2 through 4, the PIV laboratory data has a mean maximum value of 0.269 $\frac{m}{s}$ and the model predicts a mean maximum value of 0.231 $\frac{m}{s}$ or a relative error of 14.1 %. The phase in the laboratory and model agree within 4 seconds or 8 % of the tidal period [Figure 5.31].

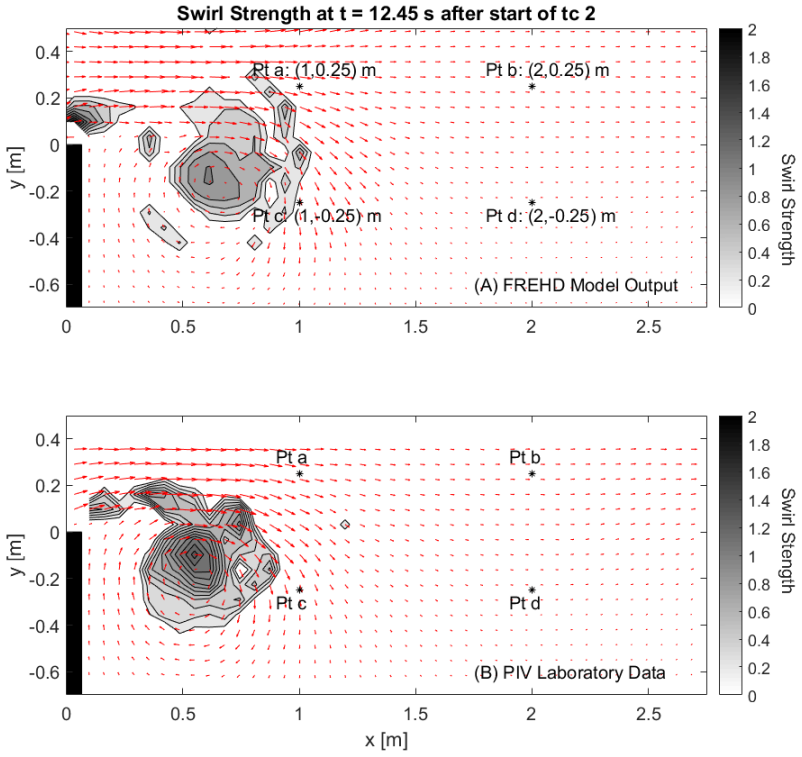

Figure 5.32: Swirl strength for (A) FREHD model with third order upwind advection scheme and (B) PIV laboratory data.

The third order upwind advection scheme predicts higher swirl strength values to occur within the model run [Figure 5.32]. The threshold that defines the vortex edge is 0.2 for both the model and PIV laboratory data. The swirl strength at one time shows

that the vortex shape changes when a higher order advection scheme is used. The primary vortex is no longer the only vortex formation within the flow. There are other vortices present within the model run similar to the secondary vortices in the PIV data. Figure 5.32 shows some smaller vortices on the right side of the vortex for the PIV lavboratory data which are most likely caused by secondary vortices merging with the primary vortex. These smaller vortices are also predicted by the FREHD model. Most likely the higher swirl strength values and possible secondary vortex formation in the model are due to a decrease in numerical dissipation when the advection scheme is improved from first order to third order.

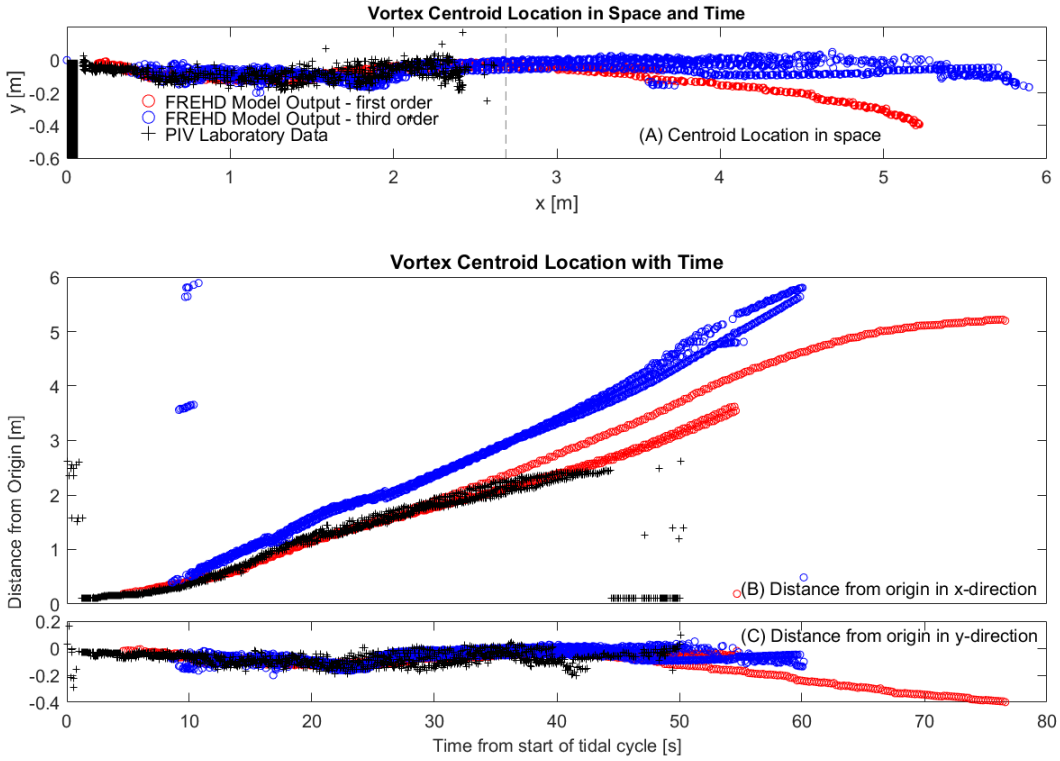

Figure 5.33: Vortex centroid location in (A) space and (B,C) time for the idealized inlet configuration with third order upwind advection scheme.

The location of the centroid is similar within the PIV field of view for both the first order and third order schemes. After the PIV field of view, the first order scheme predicts the vortex to travel toward the corner of the tank whereas the third order scheme predicts a straight trajectory [Figure 5.33a]. The vortices move faster within the third order advection scheme since the velocities within the flow fied increase when the scheme changes. The first order scheme also has more numerical dissipation than the third order scheme so the vortices travel further when the third order advection scheme is used. The difference in location of the centroid in the x direction reaches a maximum of approximately 1 m at the completion of each tidal cycle [Figure 5.33b].

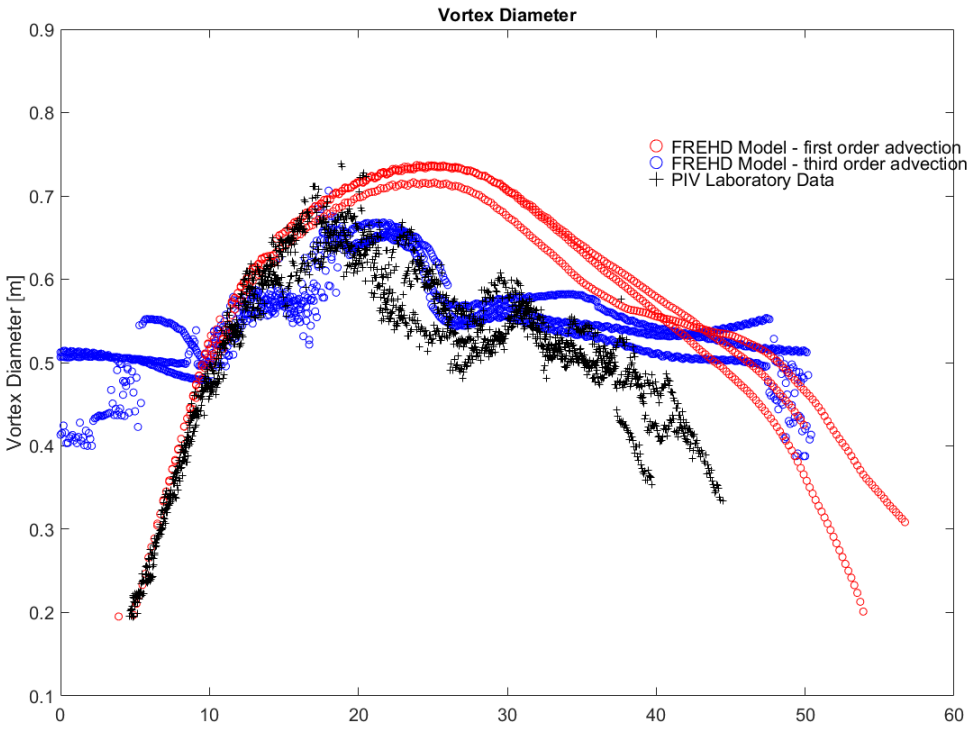

Figure 5.34: Primary vortex diameter for FREHD model with first and third order upwind advection scheme and PIV laboratory data.

The diameter of the primary vortex in the PIV laboratory data has a mean maximum value of 0.708 m and the model predicts a mean maximum value of 0.691 m. The relative error is only 2.17 %. The model also captures the shape of the diameter with time. Approximately 28 seconds after the start of each tidal cycle, the PIV laboratory data shows a decrease in the vortex diameter and then an immediate increase. At the same time the model predicts the same shape. After about 30 seconds from the start of the tidal cycle, the model has a higher diameter than the PIV laboratory data. This most likely is due to the location of the PIV field of view. The model captures the vortex formation throughout the entire domain so the diameter is able to be calculated over a longer period than the PIV laboratory data [Figure 5.34].

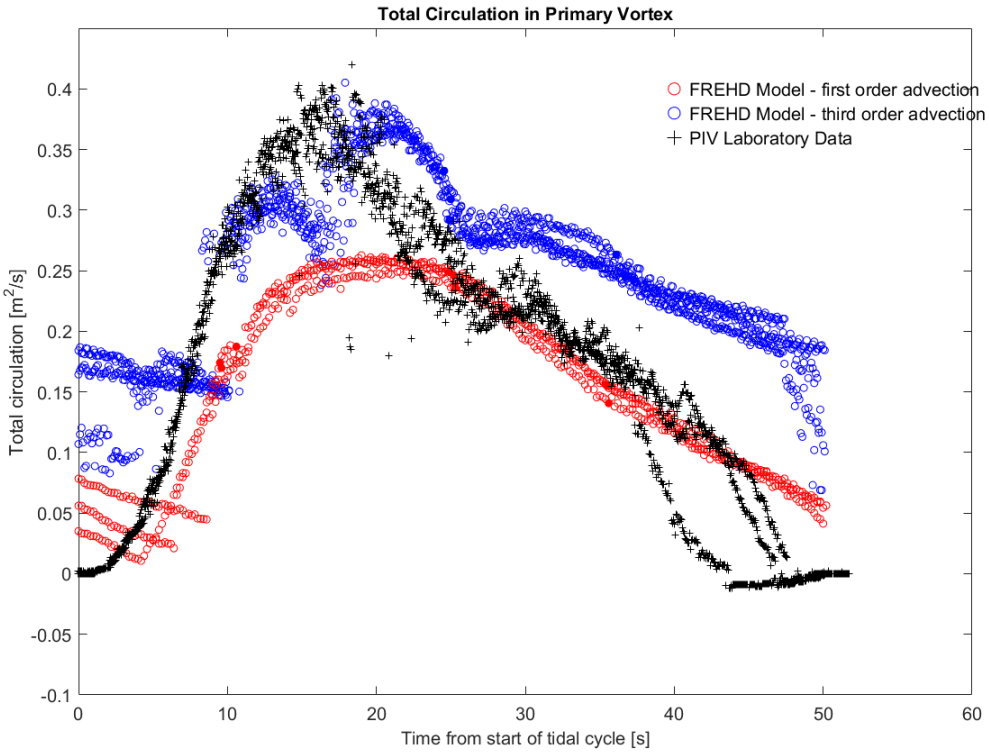

Figure 5.35: Total circulation in the primary vortex for FREHD model with first and third order upwind advection scheme and PIV laboratory data.

The total circulation within the primary vortex increases when the advection scheme is improved. The maximum total circulation for the PIV laboratory data and the FREHD model are 0.42 $\frac{m^2}{s}$ and 0.405 $\frac{m^2}{s}$ respectively. This is a relative error of 3.55 %. Although the total circulation is still lower than the PIV laboratory data, it increases by about 25% from the first order scheme. This increase can also be explained by the decreased numerical dissipation [Figure 5.35].

Overall, the third order upwind advection scheme shows the best agreement with the laboratory data. The high amount of numerical dissipation in the first order upwind

scheme limits the maximum swirl strength values possible within the model. The higher order scheme allows high swirl strength values to exist within the model as well as allowing for other vortices to form aside from the primary vortex. The hypothesis that the secondary vortex formation is vital to correctly predict the amount of circulation within the primary vortex seems to be correct. The third order upwind scheme allows for secondary vortex formation and predicts the correct amount of circulation within the primary vortex.

6 SUMMARY AND CONCLUSIONS

For tidal flow through an inlet, the velocity time histories are predicted with a 3D model (FREHD) with a one equation turbulence model, hydrostatic pressure assumption, and first order upwind advection scheme. Experimental results are presented and compared to the results from the FREHD model. The swirl strength was used to determine the location and size of the vortices in both datasets to determine the accuracy of the FREHD model in predicting vortex behavior.

The model was able to capture important characteristics of the vortices which affect the way they behave and the overall transport in and out of the inlet. The model well predicted the trajectory of the starting jet vortex for all three water depths with an idealized inlet configuration. For the three and five centimeter water depths, the model also predicted the vortex size with relative accuracy. The circulation within the primary vortex shows the correct shape but has a lower peak than shown in the experimental data. The total circulation within the primary vortex is under predicted for the first half of the tidal cycle but matches after approximately 22 seconds have passed. During this time, secondary vortices are forming and shedding from the inlet so we hypothesize that they contribute to the total circulation. For the nine centimeter water depth, the model overpredicted the size of the vortices but predicted the total circulation within the primary vortex well.

The maximum swirl strength and vorticity values within the starting-jet vortex are consistently underestimated. We predict that this is due to the inadequate resolution at the

boundary or too much numerical dissipation due to the advection scheme. Decreasing the grid size or using a higher order advection scheme results in an increase in swirl strength and vorticity within the flow field. The numerical dissipation in the first order upwind advection scheme does not allow for the high swirl strength values shown in the PIV laboratory data but a third order upwind scheme increases the maximum swirl strength and allows for smaller vortices to form aside from the primary vortex. The third order scheme also improves the agreement between the PIV laboratory data and the vortex properties predicted by the model.

Grid resolution also improves the maximum swirl strength values predicted by the model. With an extremely fine resolution along the boundary, it is predicted that the maximum swirl strength within the primary vortex would increase and approach the values seen in the experimental results. This is beneficial since many models that use an unstructured or composite grid have the ability to use an extremely fine grid in detailed portions of the domain and a coarser grid elsewhere. The FREHD model runs did prove that the trajectory and size are relatively unchanged as the grid size increases so if a finer grid is used within an inlet, these properties should remain unchanged unless vortex interaction occurs, where the strength of vorticity is important (e.g. long channels).

The model behavior allows assumptions to be made about the necessary model components needed to capture the correct behavior of starting jet vortices. The turbulence model proved to be extremely important in how the vortex behaves. A constant viscosity turbulence model is not sufficient to resolve the vortices but a one-equation turbulence

model improves the results tremendously. The sidewall friction coefficient also proved important when specifying the input parameters to the FREHD model. The sidewall friction coefficient should be present but can not exceed a certain value or friction begins to dominate the vortex behavior. The FREHD model runs and previous literature [19] suggest that the hydrostatic pressure assumption is sufficient to capture the vortex behavior. The advection scheme proved to be extremely important to the model performance.

The FREHD model could be used to determine the vortex size and trajectory for a specific inlet configuration at a field scale and then the results could be implemented into a more powerful model with a higher grid resolution. This way the transport due to the vortex behavior can be captured as well as other transport processes which are hard to implement in FREHD. Most likely wind would need to be added to the FREHD model before it was used for field scale modeling since wind-driven coastal setup plays a large role in water level variance especially at inlets along the Gulf of Mexico. Overall, the results from the FREHD model give a level of certainty that a model with the hydrostatic pressure assumption and at least a one-equation turbulence model can capture vortex formation at the mouth of an inlet.

REFERENCES

[1] R.J. Adrian, K.T. Christensen, and Z.C. Liu, "Analysis and interpretation of instantaneous turbulent velocity fields," *Experiments in Fluids*, vol. 29, pp. 275-290, Sep. 2000.

[2] M.J. Alaee, G. Ivey, and C. Pattiaratchi, "Secondary circulation induced by flow curvature and coriolis effects around headlands and islands," *Ocean Dynamics*, vol. 54, pp. 27-38, 2004.

[3] A.C. Bastos, D. Paphitis, and M.B. Collins, "Short-term dynamics and maintenance processes of headland-associated sandbanks: Shambles Bank, English Channel, UK," *Estuarine, Coastal and Shelf Science*, vol. 59, pp. 33-47, 2004.

[4] D. Bellafiore and G. Umgiesser, "Hydrodynamic coastal processes in the North Adriatic investigated with a 3D fine element model," *Ocean Dynamics*, vol. 60, pp. 255-273, 2010.

[5] D.B. Bryant, K.A. Whilden, S.A. Socolofsky, and K.-A. Chang, "Formation of tidal starting-jet vortices through idealized barotropic inlets with finite length," *Environmental Fluid Mechanics*, vol. 12, pp. 301-319, 2012.

[6] I. B. Celik, "Introductory turbulence modeling," *West Virginia University Mechanical & Aerospace Engineering Dept.*, December 1999.

[7] S. Draper, T. Stallard, P. Stansby, S. Way, T. Adcock, “Laboratory scale experiments and preliminary modelling to investigate basin scale tidal stream Energy Extraction,” in *10th European Wave and Energy Conference*, 2013.

[8] Geyer and Signell, “Measurements of tidal flow around a headland with a ship-board acoustic doppler current profiler,” *Journal of Geophysical Research*, vol. 95, pp. 3189–3197, March 1990.

[9] W. R. Geyer, “Three-dimensional tidal flow around headlands,” *Journal of Geophysical Research*, vol. 98, pp. 955–966, January 1993.

[10] G.S. Glushko, “Turbulent boundary layer on a flat plate in an imcompressible fluid,” *Izvestiia Akademii Nauk SSSR. Seriia Mekhanika*, 1965.

[11] M. Kashiwai, “Tidal residual circulation produced by a tidal vortex,” *Journal of Oceanographical Society of Japan*, vol. 40, pp. 279–294, 1984a.

[12] M. Kashiwai, “Tidal residual circulation produced by a tidal vortex part. 2 vorticity balance and kinetic energy,” *Journal of Oceanographical Society of Japan*, vol. 40, pp. 437–444, 1984b.

[13] E.J. López-Sánchez and G. Ruiz-Chavarría, “Vorticity and particle transport in periodic flow leaving a channel,” *European Journal of Mechanics B/Fluids*, vol. 42, pp. 92-103, June 2013.

[14] F. Nicolau del Roure, S.A. Socolofsky, and K-A. Chang "Structure and evolution of tidal starting jet vortices at idealized barotropic inlets," *Journal of Geophysical Research*, vol. 114, 2009.

[15] G. Pawlak, P. MacCready, K.A. Edwards, and R. McCabe, "Observations on the evolution of tidal vorticity at a stratified deep water headland," *Geophysical Research Letters*, vol. 30, no. 24, 2003.

[16] R.D. Pingree and L. Maddock, "The tidal physics of headland flow and offshore tidal bank formation," *Marine Geology*, vol. 32, pp. 269-289, 1979.

[17] R.P. Signell and W.R. Geyer, "Transient eddy formation around headlands," *Journal of Geophysical Research*, vol. 96, pp. 2561-2575, February 1991.

[18] K.C. Speirs, T.R.Healy, C.Winter, "Ebb-jet dynamics and transient eddy formation at tauranga harbour: Implications for entrance channel shoaling," *Journal of Coastal Research*, vol. 25, pp. 234–247, January 2009.

[19] P. Stansby, N. Chini, and P. Lloyd, "Oscillatory flows around a headland by 3D modelling with hydrostatic pressure and implicit bed shear stress comparing with experiment and depth-averaged modelling," *Coastal Engineering*, vol. 116, pp. 1-14, October 2016.

[20] D.C. Van Senden and J. Imberger, "Effects of initial conditions and ekman suction on tidal outflows from inlets," *Journal of Geophysical Research*, vol. 95, pp. 13,373–13,391, August 1990.

[21] M.G. Wells and G.-J.F. van Heijst, “A model of tidal flushing of an estuary by dipole formation,” *Dynamics of Atmospheres and Oceans*, vol. 37, pp. 223–244, 2003.

[22] K.A. Whilden, “Laboratory analysis of vortex dynamics for shallow tidal inlets,” *Master’s thesis, Texas A&M University*.

[23] K.A. Whilden, S.A. Socolofsky, K.-A. Chang, and J.L. Irish, “Using surface drifter observations to measure tidal vortices and relative diffusion at Aransas Pass, Texas,” *Environmental Fluid Mechanics*, vol. 14, pp. 1147–1172, 2014.

APPENDIX A

ELECTRONIC SUPPLEMENT

Visualizations of the swirl strength over time for both the PIV laboratory data and the FREHD model are included for the idealized inlet configuration for the 5 cm water depth. All movies are real time and begin with the start of the second tidal cycle. The velocity vectors are also presented on a 6.5x6.5 cm grid for both the PIV laboratory data and the FREHD model.